

# A covariant formulation for cosmological radiative transfer of the 21-cm line

Jennifer Y. H. Chan<sup>1,2,3\*</sup>, Qin Han<sup>4</sup>, Kinwah Wu<sup>4</sup> and Jason D. McEwen<sup>4</sup>

<sup>1</sup>Canadian Institute for Theoretical Astrophysics, University of Toronto, 60 St George St, Toronto, ON M5S 3H8, Canada

<sup>2</sup>Dunlap Institute for Astronomy and Astrophysics, University of Toronto, 50 St George St, Toronto, ON M5S 3H4, Canada

<sup>3</sup>Faculty of Arts and Science, University of Toronto, 100 St George St, Toronto, ON M5S 3G3, Canada

<sup>4</sup>Mullard Space Science Laboratory, University College London, Holmbury St Mary, Surrey, RH5 6NT, UK

Accepted 2024 April 19. Received 2024 April 2; in original form 2023 September 22

## ABSTRACT

The 21-cm hyperfine line of neutral hydrogen is a useful tool to probe the conditions of the Universe during the Dark Ages, Cosmic Dawn, and the Epoch of Reionisation. In most of the current calculations, the 21-cm line signals at given frequencies are computed, using an integrated line-of-sight line opacity, with the correction for cosmological expansion. These calculations have not fully captured the line and continuum interactions in the radiative transfer, in response to evolution of the radiation field and the variations of thermal and dynamic properties of the line-of-sight medium. We construct a covariant formulation for the radiative transfer of the 21-cm line and derive the cosmological 21-cm line radiative transfer (C21LRT) equation. The formulation properly accounts for local emission and absorption processes and the interaction between the line and continuum when the radiation propagates across the expanding Universe to the present observer. Our C21LRT calculations show that methods simply summing the line optical depth could lead to error of 5% in the 21-cm signals for redshift  $z \sim 12 - 35$  and of  $> 10\%$  for redshift  $z \lesssim 8$ . Proper covariant radiative transfer is therefore necessary for producing correct theoretical templates for extracting information of the structural evolution of the Universe through the Epoch of Reionisation from the 21-cm tomographic data.

**Key words:** radiative transfer – intergalactic medium – dark ages, reionisation, first stars – radio lines: general – line: formation – line profiles

## 1 INTRODUCTION

The Universe was once generally smooth and filled with neutral gas (Smoot et al. 1992; Bennett et al. 2013; Planck Collaboration XVI 2014), mainly hydrogen, but it looks very different today. The present Universe is structured, with gravitational-bound objects forming the cosmic web, a giant network of brightly-lit gas, stars and galaxies (White et al. 1987; Bond et al. 1996; de Lapparent et al. 1986; Colless et al. 2003; Tegmark et al. 2004; van de Weygaert & Schaap 2009; Huchra et al. 2012; Guzzo et al. 2014; Rien van de Weygaert et al. 2016; Libeskind et al. 2018; Bacon et al. 2021). The transition that ushered the Universe from suffusing with neutral hydrogen (HI) gas into mostly ionised plasmas – the cosmological reionisation – was driven by radiation from the first stars and galaxies, and also the first Active Galactic Nuclei (AGN) (see e.g. Barkana & Loeb 2001; Pritchard & Loeb 2012; Loeb & Furlanetto 2013; Mesinger 2016; Dayal et al. 2020; Muñoz et al. 2022). The UV radiation from the first stars and the first galaxies carved the neutral medium surrounding them into ionised cavities, and the X-rays from the first AGN, powered by accretion onto super-massive black holes, easily turned a large amount of primordial atomic gases into ionised plasmas over a

large distance. As the Universe expanded and more ionising sources emerged, these ionised cavities expanded, percolated and merged (see e.g. Gnedin 2000; Haiman & Holder 2003; Iliiev et al. 2006; McQuinn et al. 2007; Nusser 2005; Santos et al. 2008, 2010; Shin et al. 2008; Robertson et al. 2010; Mesinger et al. 2011; Geil et al. 2017; Kannan et al. 2022), allowing ionising radiation to travel further without further attenuation. The intergalactic space was gradually transformed, from being a neutral atomic fog, into a transparent sea of charged particles, leaving only some islands of neutral gas that are dense enough for self-shielding from the ionising radiation (e.g. Furlanetto & Oh 2005; Wyithe & Loeb 2008).

How the development of structures in the Universe was associated with the cosmological reionisation is a fundamental question in astrophysics. The 21-cm hyperfine line of HI is identified as a means to track the progression of cosmological reionisation processes and its interplay with the formation of luminous objects, i.e. stars, galaxies and accretion-powered compact objects (see e.g. Field 1959; Sunyaev & Zeldovich 1975; Hogan & Rees 1979; Scott & Rees 1990; Subramanian & Padmanabhan 1993; Madau et al. 1997; Barkana & Loeb 2001; Gnedin & Shaver 2004; Zaldarriaga et al. 2004; Furlanetto et al. 2006; Morales & Wyithe 2010; Pritchard & Loeb 2012; Loeb & Furlanetto 2013; Furlanetto 2016; Kulkarni et al. 2017). Observations to map the 21-cm emission across the sky over the

\* E-mail: jyhchan@cita.utoronto.ca (JYHC), qin.han.21@ucl.ac.uk (QH), kinwah.wu@ucl.ac.uk (KW), jason.mcewen@ucl.ac.uk (JDM)

evolutionary history of the Universe have been proposed, and some have already commenced, e.g. LOFAR<sup>1</sup>, MWA<sup>2</sup>, and HERA<sup>3</sup> (see e.g. Koopmans et al. 2021). With the advent of the SKA<sup>4</sup>, we will be able to carry out full-fledged all-sky 21-cm tomographic studies (Mellema et al. 2015; Koopmans et al. 2015). These all-sky data can also be used for cross analysis with other data, such as those obtained from survey observations (e.g. Furlanetto & Lidz 2007) and from line intensity mapping experiments (e.g. Lidz et al. 2009; Visbal & Loeb 2010; Lidz et al. 2011; Carilli 2011; Gong et al. 2011; Silva et al. 2013; Chang et al. 2015; Breyse et al. 2022; Silva et al. 2021). The reliability of extracting information from the 21-cm tomographic data of multi-wavelength cross-studies would depend on our understanding of the production and attenuation of the 21-cm line when it propagates from the distant Universe to us. In this work we first present a covariant formulation for the radiative transfer of the 21-cm line in an evolving and expanding Universe. The formulation takes proper account of ionisation and thermal states of the line-of-sight medium, the evolution of the intergalactic radiation field, and the cosmological expansion of the Universe. We then derive a ray-tracing scheme for cosmological radiative transfer calculations and compute the tomographic spectra of the 21-cm line in representative settings.

We organise the paper as follows. The covariant formulation of cosmological line radiative transfer is presented in Section 2, followed by the construction of the radiative transfer equation for transporting the 21-cm line radiation in a flat expanding universe and the specification of the 21-cm line transfer coefficients in Section 3. Section 4 outlines the design of the cosmological 21-cm line radiative transfer (C21LRT) all-sky algorithm and its computational structure. The setting and input reionisation history for 21-cm tomography calculations with C21LRT in this paper are described in Section 5. Section 6 presents and discusses the 21-cm tomography results with C21LRT code, compares our results with the commonly adopted optical-depth parametrisation. The importance of proper modelling of line profiles, covariant formulation for C21LRT for correct tomographic studies is also explained. Finally, we summarise the paper in Section 7.

## 2 COSMOLOGICAL LINE RADIATIVE TRANSFER

### 2.1 Line radiative transfer in the presence of continuum

In a local rest frame, the transfer equation for an unpolarised radiation of frequency  $\nu$  and specific intensity  $I_\nu$  reads

$$\frac{dI_\nu}{ds} = - \left( \kappa_{C,\nu} + \kappa_{L,\nu}^{\text{abs}} \phi_{\nu,\text{abs}} - \kappa_{L,\nu}^{\text{sti}} \phi_{\nu,\text{sti}} \right) I_\nu + (\epsilon_{C,\nu} + \epsilon_{L,\nu} \phi_{\nu,\text{emi}}) \quad (1)$$

(cf. Wu et al. 2001), where  $s$  is the photon's path length. The subscript ‘‘C’’ denotes the continuum underneath and neighbouring to the line, ‘‘L’’ denotes the line centre. The absorption coefficient  $\kappa_\nu$  has three components, contributed by the absorption of the line and the continuum and the stimulated emission (which can be considered as a negative absorption) of the line; the emission coefficient  $\epsilon_\nu$  has two components, contributed by the emission of the line and the continuum. The line profile functions  $\phi_{\nu,x} \equiv \phi_x(\nu - \nu_{\text{line},0})$ , with  $x \in \{\text{abs}, \text{emi}, \text{sti}\}$  corresponding to absorption, spontaneous

emission and stimulated emission, respectively, are defined with respect to the rest-frame frequency of the emission line, and they are normalised, i.e.

$$\int_0^\infty d\nu \phi_{\nu,x} = \int_0^\infty d\nu \phi_x(\nu - \nu_{\text{line},0}) = 1, \quad (2)$$

where  $\nu_{\text{line},0}$  is the intrinsic line frequency, corresponding the energy difference between two states in the transition, in the rest frame. This radiative transfer equation is valid if the continuum at the line and its neighbouring frequencies does not show strong variations, e.g. no absorption edge. It is applicable if photon scattering and energy redistribution between the electronic states are unimportant. This line profile function gives the strength of the line, in the context of absorption, spontaneous emission and stimulated emission.

Hereafter the notation, the subscript ‘‘ $\nu$ ’’ of the frequency-dependent quantities are dropped, unless otherwise stated, for better clarity in the expressions. Without losing generality, suppose that the line has a symmetric profile about its intrinsic line frequency, At the line centre, the transfer equation (Eqn. (2)) takes the form

$$\frac{dI_L}{ds} = - \left( \kappa_C + \kappa_L^{\text{abs}} - \kappa_L^{\text{sti}} \right) I_L + (\epsilon_C + \epsilon_L) \quad (3)$$

(see Tucker 1977; Wu et al. 2001). The transfer processes are determined by an opacity contributed jointly by the line and the continuum. As the continuum is slowly varying with frequency, the radiative transfer of the continuum at the line frequencies can be approximated by the radiative transfer of the continuum at the neighbouring frequencies where the line profile function is insignificant, i.e.  $\phi_\nu \ll 1$ . This gives the continuum radiative transfer equation:

$$\frac{dI_C}{ds} = -\kappa_C I_C + \epsilon_C, \quad (4)$$

in which only the opacity of the continuum contributes to the transfer process.

Whether the line appears as an emission feature or an absorption feature depends on the relative strength of  $I_L$  and  $I_C$ , if the line is centrally peaked. The line appears as emission when  $I_L > I_C$ , and in absorption when  $I_L < I_C$ .

### 2.2 Covariant formulation for generic line radiative transfer

Radiative transfer in a cosmological setting needs to firstly account for the expansion of the Universe. It needs to account also for the frequency redistribution in the radiative processes and the complex structures in the frequency shifted and stretched line profile. The covariant form of the radiative transfer equation is given by

$$\frac{d}{d\lambda_a} \left( \frac{I_\nu}{\nu^3} \right) \Big|_{\lambda_a, \text{co}} = -k_\alpha u^\alpha \Big|_{\lambda_a, \text{co}} \left\{ -\kappa_{\text{tot},\nu} \left( \frac{I_\nu}{\nu^3} \right) + \frac{\epsilon_{\text{tot},\nu}}{\nu^3} \right\} \quad (5)$$

(see Younsi et al. 2012; Chan et al. 2019), which is derived from the conservation of phase space density and the conservation of photon number. Here all the quantities are frequency dependent and are evaluated in a comoving reference frame (denoted by the subscript ‘‘co’’) along the path of a photon. If the processes that give rise to the opacity of the line and the continuum are independent, the absorption and emission coefficients can be expressed as the sum of the contributions of the relevant processes, i.e.  $\kappa_{\text{tot},\nu} = \kappa_{C,\nu} + \tilde{\kappa}_{L,\nu}$  and  $\epsilon_{\text{tot},\nu} = \epsilon_{C,\nu} + \tilde{\epsilon}_{L,\nu}$ , respectively. The factor  $k_\alpha u^\alpha$  is arisen from evaluating the variation in the photon's path length  $s$  with respect to the affine parameter  $\lambda_a$  for a photon with a 4-momentum  $k^\alpha$  propagating in a cosmological medium that has 4-velocity  $u^\beta$ . In

<sup>1</sup> <https://www.astron.nl/telescopes/lofar/>

<sup>2</sup> <https://www.mwatelescope.org/>

<sup>3</sup> <https://reionization.org/>

<sup>4</sup> <https://www.skatelescope.org/>

cosmological radiative transfer,  $k_\alpha u^\alpha$  is determined by the space-time metric of a chosen cosmological model. As such, Eqn. (5) can be evaluated in terms of a cosmological variable instead of the affine parameter  $\lambda_a$  (see Fuerst & Wu 2004). In a flat Friedmann–Lemaître–Robertson–Walker (FLRW) universe, the metric has diagonal elements  $(-1, a^2, a^2, a^2)$ , where  $a = 1/(1+z)$  is the cosmological scale factor and  $z$  is the cosmological redshift. For a photon of 4-momentum  $k^\alpha$  ( $k^\alpha = (E/c, \mathbf{p})$  where  $\mathbf{p} = (p_r, p_\theta, p_\phi)$  denotes the 3-velocity of the photon) propagating in a cosmological medium with 4-velocity  $u^\beta$  ( $u^\beta = \gamma(1, \boldsymbol{\beta})$  where  $\boldsymbol{\beta} = (\beta_r, \beta_\theta, \beta_\phi)$  denotes the 3-velocity of the medium and  $\gamma = 1/\sqrt{1+\beta^2}$  is the corresponding Lorentz factor) to the observer,

$$k_\alpha u^\alpha \Big|_z = \gamma_z v_z (-1 + a^2 \beta_{r,z}), \quad (6)$$

where we have used the convention that the speed of light and the Planck constant have numeric value 1 (i.e.,  $c = h = 1$ ) here. If the motion of the line-of-sight medium is insignificant (i.e.  $\beta = 0$  and  $\gamma=1$ ), the ratio of  $k_\alpha u^\alpha$  evaluated at an earlier epoch to that at the present day is the relative shift of energy (or frequency) of the photon, i.e.

$$\frac{k_\alpha u^\alpha \Big|_z}{k_\beta u^\beta \Big|_{z_{\text{obs}}}} = \frac{v_z}{v_{z_{\text{obs}}}} = \frac{a_{\text{obs}}}{a} = \frac{1+z}{1+z_{\text{obs}}}. \quad (7)$$

Note that in an expanding flat universe, locally at a redshift  $z$ , we may express the derivative by

$$\frac{d}{d\lambda_a} \Big|_z = \frac{dx^0}{d\lambda_a} \frac{d}{dx^0} \Big|_z = E \frac{d}{ds} \Big|_z = \left( E \frac{dz}{ds} \right) \Big|_z \frac{d}{dz}, \quad (8)$$

where  $k^\alpha = (E/c, \mathbf{p}) = dx^\alpha/d\lambda_a$ . It follows, from Eqn. (5), that the covariant line radiative transfer equation for a flat FLRW Universe is

$$\frac{d}{dz} \left( \frac{I_\nu}{\nu^3} \right) = (1+z) \left[ -(\kappa_{C,\nu} + \tilde{\kappa}_{L,\nu}) \left( \frac{I_\nu}{\nu^3} \right) + \frac{(\epsilon_{C,\nu} + \tilde{\epsilon}_{L,\nu})}{\nu^3} \right] \frac{ds}{dz}. \quad (9)$$

Here, the line absorption coefficient  $\tilde{\kappa}_{L,\nu}$  and the line emission coefficient  $\tilde{\epsilon}_{L,\nu}$  account for the line profile, specified at a fixed redshift. These transfer coefficients are macroscopic variables, but governed by microscopic processes. The increment of path length with respect to the change in redshift is

$$\frac{ds}{dz} = \frac{c}{H_0} (1+z)^{-1} \left[ \Omega_{r,0} (1+z)^4 + \Omega_{m,0} (1+z)^3 + \Omega_{\Lambda,0} \right]^{-1/2} \quad (10)$$

(see e.g. Peacock 1999), where  $H_0$  is the Hubble parameter,  $\Omega_{r,0}$ ,  $\Omega_{m,0}$  and  $\Omega_{\Lambda,0}$  are the dimensionless energy densities of relativistic matter and radiation, non-relativistic matter, and a cosmological constant (dark energy with an equation of state of  $w \equiv -1$ ), respectively. The subscript “0” here indicates that the quantities are measured at the present epoch (i.e.  $z = 0$ ).

### 3 COSMOLOGICAL 21-CM LINE RADIATIVE TRANSFER

Here we present the cosmological transport specific to the 21-cm line of HI in the presence of a background continuum radiation such as the cosmic microwave background (CMB). We also provide a pedagogical discussion about the global and local line shifting and line broadening effects that a line radiation would be subjected to in a general physical settings.

#### 3.1 The 21-cm line transfer equation and transfer coefficients

The 21-cm line absorption and emission are determined by the probability of the transition between the hyperfine states (“u” for the higher-energy triplet  $1_1S_{1/2}$  state, and “l” for the lower-energy  $1_0S_{1/2}$  singlet state) due to the spin-flip of the ground state electron in the HI. The transition between the two spin states is a magnetic dipole transition. It is mediated by the emission or absorption of a photon of an energy difference between the two hyperfine levels, i.e.  $\Delta E_{ul} = h\nu_{ul} = 5.87 \times 10^{-6}$  eV, corresponding to a wavelength of 21.1 cm and a frequency of  $\nu_{21\text{cm}} = 1.42$  GHz (Hellwig et al. 1970; Essen et al. 1971). The line profile functions for the HI hyperfine line are therefore  $\phi_x(\nu - \nu_{\text{line},0}) = \phi_x(\nu - \nu_{21\text{cm}})$ , where  $x \in \{\text{abs, emi, sti}\}$ .

The transition probabilities of the absorption, spontaneous emission and stimulated emission of a photon with  $\Delta E_{ul}$  are specified by the Einstein coefficients  $B_{lu}$ ,  $A_{ul}$  and  $B_{ul}$ , respectively. Consider an ensemble of HI atoms in the 1S ground state, with the populations of electrons in its triplet and singlet spin states specified by the number densities  $n_u$  and  $n_l$ , respectively. Thus, the effective emission coefficient of the 21-cm line may be expressed as

$$\epsilon_{21\text{cm}} = \epsilon_{ul} = \frac{h\nu_{ul}}{4\pi} n_u A_{ul} \int_0^\infty d\nu \phi_{\nu,\text{emi}}. \quad (11)$$

Similarly, the expression for the effective absorption coefficient of the 21-cm line is

$$\begin{aligned} \kappa_L &= \kappa_{21\text{cm}}^{\text{abs}} - \kappa_{21\text{cm}}^{\text{sti}} \\ &= \kappa_{ul}^{\text{abs}} - \kappa_{ul}^{\text{sti}} \\ &= \frac{h\nu_{ul}}{4\pi} \left[ n_l B_{lu} \int_0^\infty d\nu \phi_{\nu,\text{abs}} - n_u B_{ul} \int_0^\infty d\nu \phi_{\nu,\text{sti}} \right]. \end{aligned} \quad (12)$$

It follows that the specific emission and absorption coefficients are

$$\epsilon_{L,\nu} = \frac{h\nu_{ul}}{4\pi} n_u A_{ul} \phi_{\nu,\text{emi}}; \quad (13)$$

$$\kappa_{L,\nu} = \frac{h\nu_{ul}}{4\pi} \left[ n_l B_{lu} \phi_{\nu,\text{abs}} - n_u B_{ul} \phi_{\nu,\text{sti}} \right]. \quad (14)$$

For a two-level system in thermal equilibrium, characterised by a thermal temperature  $T$ , the relative population of the particles at the two levels differing by an energy  $\Delta E_{ba}$  (with labels “b” and “a” for the levels with the higher energy and lower energy, respectively), is specified by the Boltzmann factor:

$$\frac{n_b}{n_a} = \frac{g_b}{g_a} \exp\left(-\frac{\Delta E_{ba}}{k_B T}\right), \quad (15)$$

where  $k_B$  is the Boltzmann constant. Analogous to the expression for the thermal system, the relative population of the upper and lower hyperfine states of the 21-cm line may be expressed in terms of a temperature,  $T_s$ , known as the spin temperature (Field 1958):

$$\frac{1}{3} \left( \frac{n_u}{n_l} \right) = \exp\left(-\frac{\Delta E_{ul}}{k_B T_s}\right) = \exp\left(-\frac{T_\star}{T_s}\right), \quad (16)$$

with  $g_u = 3g_l$  (for HI in the 1S ground state) and  $T_\star \equiv h\nu_{21\text{cm}}/k_B = \Delta E_{ul}/k_B = 0.0682$  K. Note that when  $T_s \gg T_\star$ , three of four atoms will be in the upper hyperfine level. However, there are mechanisms that can cause violation of this population partition. For example, Ly $\alpha$  pumping will allow a higher number of HI atoms in the upper hyperfine state through the Wouthuysen-Field mechanism (Wouthuysen 1952; Field 1958). Collisional excitation is important in establishing the population of electrons in the upper hyperfine state in the absence of an external radiation field. The collision rate between

particles generally increases with the square of particle number densities. Collisional excitation and de-excitation are, therefore, particularly important in high-density environments. Collisions could be the dominant process for the hyperfine transitions during the Dark Ages. However, they would give way to the radiative processes, when the first luminous objects began to appear. High-frequency radio background radiation at a high  $z$  can be redshifted into the frequency of the 21-cm line, causing absorption or inducing stimulated emission. The background radio sources can be the diffuse ambient CMB, but can also be strong radio emitters, such as quasars.

Without loss of generality, consider only the line absorption and emission and ignore the continuum and its opacity for the time being. Then, the radiative transfer equation is simply

$$\frac{dI_\nu}{ds} = -\kappa_{L,\nu} I_\nu + \epsilon_{L,\nu} = -\kappa_{L,\nu} (I_\nu - S_{L,\nu}) \quad (17)$$

in the local rest frame, where  $S_{L,\nu} = \epsilon_{L,\nu}/\kappa_{L,\nu}$  is the source function of the line. (This can be justified if the free-free processes, which usually contribute to the continuum emission and absorption, are insignificant, i.e.  $\kappa_{C,\nu} \ll \kappa_{L,\nu}$  and  $\epsilon_{C,\nu} \ll \epsilon_{L,\nu}$ .) In terms of the Einstein coefficients, the radiative transfer equation for the 21-cm line, therefore, is

$$\frac{dI_\nu}{ds} = -\frac{h\nu_{ul}}{4\pi} \left[ (n_l B_{lu} \phi_{\nu,abs} - n_u B_{ul} \phi_{\nu,sti}) I_\nu - n_u A_{ul} \phi_{\nu,emi} \right], \quad (18)$$

where  $\nu_{ul} = \nu_{21cm}$ , and the source function is

$$\begin{aligned} S_{L,\nu} &= \frac{n_u A_{ul} \phi_{\nu,emi}}{n_l B_{lu} \phi_{\nu,abs} - n_u B_{ul} \phi_{\nu,sti}} \\ &= \left( \frac{A_{ul}}{B_{ul}} \right) \frac{(\phi_{\nu,emi}/\phi_{\nu,abs})}{(n_l B_{lu}/n_u B_{ul}) - (\phi_{\nu,sti}/\phi_{\nu,abs})} \\ &= \left( \frac{2h\nu_{ul}^3}{c^2} \right) \frac{(\phi_{\nu,emi}/\phi_{\nu,abs})}{(n_l g_u/n_u g_l) - (\phi_{\nu,sti}/\phi_{\nu,abs})}. \end{aligned} \quad (19)$$

The derivation of the source function here has not assumed a thermal equilibrium. If local thermal equilibrium (LTE) is imposed, the source function will become the Planck function  $B_\nu(T)$ , recovering Kirchhoff's Law. It then follows that,

$$\frac{n_u}{n_l} = \frac{g_u}{g_l} \exp\left(-\frac{h\nu_{ul}}{k_B T}\right),$$

and the source function in Eqn. (19) becomes

$$S_{L,\nu} = \left( \frac{2h\nu_{ul}^3}{c^2} \right) \left[ \exp\left(\frac{h\nu_{ul}}{k_B T}\right) - 1 \right]^{-1} = B_\nu(T).$$

The condition for a LTE between the radiation and the medium is not always satisfied, especially when the transition is coupled with an external radiative process. In this situation,

$$\frac{n_u}{n_l} \neq \frac{g_u}{g_l} \exp\left(-\frac{h\nu_{ul}}{k_B T}\right),$$

and the source function cannot be represented by the Planck function, i.e. the radiation is non-thermal, although the relevant radiative processes involved could be thermal processes themselves.

The line transfer equation can be further simplified using the relations between the Einstein coefficients in the absorption coefficient. With

$$\frac{B_{lu}}{B_{ul}} = \frac{g_u}{g_l}, \quad \text{and} \quad \frac{A_{ul}}{B_{ul}} = \frac{2h\nu^3}{c^2} \Big|_{\nu=\nu_{ul}} \quad (20)$$

(Einstein 1916, 1917), the absorption coefficient can be expressed as

$$\begin{aligned} \kappa_{L,\nu} &= \frac{h\nu_{ul}}{4\pi} (n_l B_{lu} \phi_{\nu,abs} - n_u B_{ul} \phi_{\nu,sti}) \\ &= \kappa_{L,\nu}^{abs} \phi_{\nu,abs} (1 - \Xi), \end{aligned} \quad (21)$$

where the normalised absorption coefficient is

$$\kappa_{L,\nu}^{abs} = \frac{h\nu_{ul}}{4\pi} n_l B_{lu} = \frac{1}{8\pi} \left( \frac{c}{\nu_{ul}} \right)^2 \left( \frac{g_u}{g_l} \right) n_l A_{ul}, \quad (22)$$

and the factor for the stimulated emission is

$$\Xi = \frac{n_u g_l \phi_{\nu,sti}}{n_l g_u \phi_{\nu,abs}}. \quad (23)$$

The factor  $\Xi$  can exceed unity if the upper hyperfine level is sufficiently populated, i.e. when  $(n_u/n_l) > (g_u/g_l) = 3$  for  $\phi_{\nu,sti} = \phi_{\nu,abs}$ . This could occur during the Epoch of Reionisation (EoR) where a strong radiation field can be created by the first quasars, the first stars, or the first galaxies.

It is now clear that the emission and absorption coefficients of the radiative transfer of the hyperfine 21-cm line of HI can be computed from the Einstein coefficient  $A_{ul}$ , for spontaneous emission, if the number density of HI (which is  $n_u + n_l$ ) and the ratio of  $n_u/n_l$  (given by the spin temperature  $T_s$ ) are known, and the line profile functions  $\phi_{\nu,x}$ , with  $x \in \{\text{abs}, \text{emi}, \text{sti}\}$  are specified.

The line profile functions depend only on the properties of the emitting and absorbing gas. Generally, there is no guarantee that the line profile functions  $\phi_{\nu,emi}$ ,  $\phi_{\nu,abs}$ , and  $\phi_{\nu,sti}$  are the same. However, the intrinsic width of the 21-cm hyperfine line is insignificant in comparison to the broadening of the line due to other processes. In a local rest frame, all atoms are subject to the same external line broadening processes. Thus the same line profile function is used for absorption, spontaneous emission and stimulated emission, i.e.  $\phi_{\nu,emi} = \phi_{\nu,abs} = \phi_{\nu,sti} = \phi_\nu$ , in the radiative transfer equation. The continuum and line absorption and emission coefficients are additive, when there is no correlation between the continuum and the line opacities. Hence, the radiative transfer equation is

$$\frac{dI_\nu}{ds} = -\left( \kappa_{C,\nu} + \kappa_{L,\nu}^{abs} \phi_\nu [1 - \Xi] \right) I_\nu + (\epsilon_{C,\nu} + \epsilon_{L,\nu}), \quad (24)$$

where the contribution of stimulated emission  $(1 - \Xi)$  is written out explicitly for clarity.

The covariant formulation of the cosmological transport of a generic line derived in § 2.2, when applied to the 21-cm line of HI, gives the C21LRT equation:

$$\frac{d}{dz} \left( \frac{I_\nu}{\nu^3} \right) = (1+z) \left[ -(\kappa_{C,\nu} + \kappa_{L,\nu}) \left( \frac{I_\nu}{\nu^3} \right) + \frac{(\epsilon_{C,\nu} + \epsilon_{L,\nu})}{\nu^3} \right] \frac{ds}{dz}, \quad (25)$$

(cf. Eqn. (9)). Here, all the line transfer coefficients are as defined above (Eqn. (13), Eqn. (22), and Eqn. (23)), with the line profile functions substituted by the same  $\phi_\nu$ .

## 3.2 Shaping the profile of the 21-cm line

### 3.2.1 Line Shifting

When an emitting medium and the observer are not co-located and do not co-move, the frequency of the emitted radiation will appear to be shifted as seen by the observer. For the hyperfine 21-cm line from distant astrophysical systems, the shift of the line can be caused by (i) cosmological expansion, and (ii) the relative velocity between the sources and the observer.

The former is a global effect. It leads to a redshift of the frequency of the radiation, and it can be manifested in the shift of centre frequency of the hyperfine 21-cm line to a lower frequency at the observer's reference frame. Quantitatively, the relative frequency shift at two cosmological locations or epochs  $z$  and  $z'$  is given by

$$\frac{\nu(z')}{1+z'} = \frac{\nu(z)}{1+z}. \quad (26)$$

In the context of radiative transfer and spectral evolution, the frequency redshift of radiation caused by cosmological expansion is essential to a flow of photons from the high frequencies to the low frequencies at a constant rate if evaluated in terms of the cosmological redshift  $z$ .

The latter is associated with the local movement of the emitter with respect to the observer. The frequency shift is simply a Doppler effect. In the non-relativistic limit, the frequency of the centre of the observed 21-cm line  $\nu'$  is

$$\nu'_{21\text{cm}} = \nu_{21\text{cm}} (1 \pm v_{\parallel}/c), \quad (27)$$

where  $v_{\parallel}$  is the relative line-of-sight velocity of the HI gas with respect to the observer.  $v_{\parallel}$  can be positive or negative. The 21-cm line will be shifted to higher frequencies if the emitting HI gas is approaching, and to lower frequencies if the emitting HI gas is receding with respect to the observer.

### 3.2.2 Line broadening and line profile

The 21-cm hyperfine line is broadened by radiative damping, particle collision, thermal motion and turbulence. The first two are intrinsic to individual emitters, where the line emission processes are effectively damped oscillations. The last two are manifestations of Doppler effect, caused by the incoherent movements of a collection of HI gas particles with respect to the observer.

The damped oscillations associated with the emission process will lead to the broadening of the 21-cm hyperfine line, resulting in a Lorentzian profile (see e.g. [Rutten 2003](#)):

$$\phi(\nu - \nu_{21\text{cm}}) = \frac{1}{\pi} \left[ \frac{\Gamma_{\text{all}}/4\pi}{(\nu - \nu_{21\text{cm}})^2 + (\Gamma_{\text{all}}/4\pi)^2} \right], \quad (28)$$

where  $\Gamma_{\text{all}}$  is the sum of the damping parameters (i.e. reciprocals of the damping timescales) of all the uncorrelated damping processes. Spontaneous emission and collision-induced emission are independent processes, and hence, their combined broadening will be specified by a total damping parameter

$$\Gamma_{\text{all}} = \Gamma_{\text{rad}} + \Gamma_{\text{coll}} \propto \left( \frac{1}{t_{\text{rad, spon}}} + \frac{1}{t_{\text{rad, coll}}} \right), \quad (29)$$

where  $t_{\text{rad, spon}} (= 1/A_{\text{ul}})$  and  $t_{\text{rad, coll}}$  are the timescales for the spontaneous emission and for the collision-induced emission, respectively. During the EoR, the Universe was sufficiently dense such that the timescale of collisional de-excitation was significantly shorter than the timescale for spontaneous emission<sup>5</sup>, implying that  $\Gamma_{\text{coll}} \gg \Gamma_{\text{rad}}$ . The total broadening of the two processes combined is, therefore,  $\Gamma_{\text{all}} \approx \Gamma_{\text{coll}}$ , corresponding to a full-width-half-maximum

<sup>5</sup> The collisional timescale is inversely proportional to the density of the gas. The relative importance of collisional damping and radiative damping is, therefore, environment dependent in the 21-cm hyperfine transition. While collisional damping dominated in HI gas suffusing the early Universe, it is less important in the present-day intergalactic medium.

(FWHM) in frequency,  $\text{FWHM}_{\nu}$ , of  $(\Gamma_{\text{coll}}/2\pi)$  in the Lorentzian line profile.

The thermal motion and turbulent motion of the gas particles will give rise to Doppler shifts in the radiation that they emit. The incoherent Doppler shifts of the 21-cm line emitted from an ensemble of HI gas particles with different line-of-sight velocities would make the line appear to be broadened. When the HI gas particles have a Gaussian velocity distribution, the line will have a Gaussian profile:

$$\phi(\nu - \nu_{21\text{cm}}) = \frac{1}{\sqrt{\pi} \Delta\nu_{\text{D}}} \exp \left[ - \left( \frac{\nu - \nu_{21\text{cm}}}{\Delta\nu_{\text{D}}} \right)^2 \right]. \quad (30)$$

Suppose that the turbulent motion in a HI gas has a well-defined characteristic mean-square velocity,  $v_{\text{turb}}^2$ . Then, a velocity dispersion can be assigned for the HI gas particles, analogous to the thermal velocity dispersion, and from it, a Maxwellian velocity distribution can be constructed. As thermal motion and turbulent motion are independent, their velocity dispersions are additive. The effective width of the broadened line is

$$\Delta\nu_{\text{D}} \equiv \nu_{21\text{cm}} \left( \frac{b_{\text{D}}}{c} \right) = \nu_{21\text{cm}} \sqrt{\frac{2k_{\text{B}}T_{\text{k}}}{mc^2} + \left( \frac{v_{\text{turb}}}{c} \right)^2}, \quad (31)$$

where

$$b_{\text{D}} = \sqrt{\frac{2k_{\text{B}}T_{\text{k}}}{m} + v_{\text{turb}}^2} \quad (32)$$

is the Doppler parameter. For a Gaussian profile function, the line has a  $\text{FWHM}_{\nu} = 2\sqrt{\ln 2} b_{\text{D}}$  in velocity. In frequency,

$$\begin{aligned} \text{FWHM}_{\nu} &= 2\sqrt{\ln 2} (\nu_{21\text{cm}}) \left( \frac{b_{\text{D}}}{c} \right) \\ &= 2\sqrt{\ln 2} (\nu_{21\text{cm}}) \sqrt{\frac{2k_{\text{B}}T_{\text{k}}}{mc^2} + \left( \frac{v_{\text{turb}}}{c} \right)^2}. \end{aligned} \quad (33)$$

The damping-induced line broadening is associated with the internal action and response of the emitters; the velocity-induced line broadening is associated with the kinetics of the emitters. These two broadening are different by nature. Their effects are not additive, despite that damping and velocity-induced broadening are independent. The total broadening will be determined by a convolution when both broadening processes are present. The convolution of a Lorentzian line profile and a Gaussian line profile is a Voigt line profile. Although Voigt profiles do not have simple analytic form in terms of elementary functions (see e.g. [Schreier 1992](#); [Boyer & Lynas-Gray 2014](#); [Mohankumar & Sen 2019](#); [Aiomar 2020](#)), the normalised Voigt profile for the 21-cm line can be expressed as an implicit function of frequency  $\nu$  specified by three parameters: the line frequency centre,  $\nu_{21\text{cm}}$ , the damping parameter,  $\Gamma_{\text{all}}$ , and velocity-induced width,  $\Delta\nu_{\text{D}}$  (see [Rutten 2003](#); [Chan 2020](#)). In the astrophysical environments during cosmological reionisation, damping-induced broadening is unimportant when compared with velocity-induced broadening<sup>6</sup>. Thus, a Gaussian line profile is

<sup>6</sup> Velocity-induced broadening is predominant in high-temperature, low-pressure environments where the thermal motion of particles is significant. Damping-induced broadening becomes more comparable or dominant in dense, high-pressure environments with frequent particle collisions but the temperature affecting the velocity of the particles must not be too high. In the context of cosmological reionisation eras probed by the 21-cm line, the low density of the IGM makes velocity-induced broadening the primary mechanism. While damping-induced broadening may increase in regions with higher densities due to structure formation, rising gas temperatures due to radiation from these first luminous structures further enhance velocity broadening. Thus, our radiative transfer calculations primarily focus on velocity-induced broadening.

adopted in our subsequent radiative transfer calculations. By doing this, we let the emission or absorption distributes over an effective frequency range  $\sim(\nu_{21\text{cm}}-\text{FWHM}_\nu, \nu_{21\text{cm}}+\text{FWHM}_\nu)$ . Then the emission and coefficients at line centre  $\kappa_{L,\nu_{21\text{cm}}}$  and  $\epsilon_{L,\nu_{21\text{cm}}}$  are inversely proportional to  $\text{FWHM}_\nu$ . The emission or absorption integrated over the full relevant frequency range for a given line profile is conserved.

### 3.3 Continuum radiation background

Determination of the tomographic 21-cm line signal requires simultaneously and self-consistently solving the radiative transfer of the line (i.e. Eqn. (25)) and the radiative transfer of the continuum:

$$\frac{d}{dz} \left( \frac{I_\nu}{\nu^3} \right) = (1+z) \left[ -\kappa_{C,\nu} \left( \frac{I_\nu}{\nu^3} \right) + \frac{\epsilon_{C,\nu}}{\nu^3} \right] \frac{ds}{dz}. \quad (34)$$

The omnipresence of the CMB photons provide the radiation background that must be accounted for when looking at the cosmological 21-cm line. The CMB's spectra at different redshifts are well described by the Planck function at its characteristic temperature  $T_{\text{CMB}}(z) = T_{\text{CMB},0}(1+z)$ , with  $T_{\text{CMB},0} = 2.73$  K (Penzias & Wilson 1965; Mather et al. 1994; Spergel et al. 2003; Planck Collaboration XVI 2014).

In addition to the CMB, diffuse continuum radiation can arise from local free-free processes and synchrotron radiation. The continuum absorption ( $\kappa_{C,\nu}$ ) and emission ( $\epsilon_{C,\nu}$ ) coefficients for the thermal free-free process and the non-thermal synchrotron radiation appropriate for the studies of cosmic plasmas are discussed in Section 2.4 of Chan et al. (2019), with their explicit expressions presented in Appendix C of that paper and references therein. The absorption and emission in the continuum at frequencies of the line and adjacent to the line are less relevant, although electron scattering could cause a certain degree of extinction when the line photons traverse the ionised matter along the line-of-sight. To isolate the 21-cm line emission and absorption, which is the focus of this work, the continuum emission and absorption are assumed to be zero.

In the presence of a continuum background of a bright source, e.g. a radio-loud quasar whose emission is generally non-thermal synchrotron radiation from relativistic electrons and it tends to have a very high brightness temperature (e.g. Willott et al. 1998; Vernstrom et al. 2018), the 21-cm line will appear as absorption. Distant quasars have been identified as candidate sources for the detection of 21-cm forests (Carilli et al. 2002; Furlanetto & Loeb 2002; Furlanetto 2006; Xu et al. 2009; Mack & Wyithe 2012; Ciardi et al. 2015), where photons emitted at frequencies  $\nu > \nu_{\text{ul}}$  by the bright background radio quasar at redshift  $z_{\text{emi}}$  are absorbed by the diffuse HI gas along the line-of-sight at redshift  $z = [\nu_{\text{ul}}(1+z_{\text{emi}})/\nu - 1]$ . Other candidate bright point sources would be hypernovae, which show gamma-ray burst, with radio afterglows, and some could be fast radio burst (FRB) sources. However, little is known about the number distribution of hypernovae and FRBs and their evolution at very high redshifts, such as  $z \sim 6$  or higher.

### 3.4 Differential brightness

The 21-cm line is observed against a continuum background, which is generally sourced from the CMB, and occasionally from bright radio sources. The observed differential brightness temperature is

$$\delta T_{\text{b}} = (I_{L,\nu} - I_{C,\nu}) \frac{(c/\nu)^2}{2k_{\text{B}}}, \quad (35)$$

where we have used the Rayleigh-limit approximation. In a self-consistent manner,  $I_{L,\nu}$  is accurately determined by Eqn. (25) while  $I_{C,\nu}$  by Eqn. (34).

## 4 NUMERICAL RADIATIVE TRANSFER

### 4.1 Ray-Tracing Scheme

The C21LRT calculations consist of three key elements: (i) a ray-tracing algorithm accounting for the transport of radiation from the past to the observer in an expanding Universe, (ii) a computational component to determine the interaction between the incoming background radiation and the local medium and to evaluate the absorption of the incoming background radiation and emission in the local medium, and (iii) a numerical solver for the C21LRT equation (Eqn. (25)) and the transfer equation of the continuum (Eqn. (34)) along with the ray-tracing calculations.

On cosmological scales, the transfer of radiation along a line of sight is the transfer of radiation from the past to the present. C21LRT calculations for a single ray will provide a tomographic 21-cm spectrum at the observer epoch  $z = 0$  (or at any arbitrary redshift from the line emission epoch). Pencil-beam calculations can also be performed wherein a bundle of rays labelled by their spatial markers are traced over their path (stamped by comic time) as they traverse through an extended medium, producing a map that represents a collection of end-points of the path-integrated rays. Each of these end-points is associated with its own tomographic 21-cm spectrum that would be observed today at  $z = 0$ . In an all-sky setting, each ray can be marked by  $(\theta, \phi)$  that corresponds to its celestial sky coordinates and the radial axis  $r$  that corresponds to the redshift axis  $z$ . The C21LRT equation is then solved in a spherical polar coordinate system  $(r, \theta, \phi)$ , as in the all-sky polarised radiative transfer calculations of Chan et al. (2019).

In the covariant formulation constructed for the C21LRT calculations, the emission and absorption processes are evaluated in a local rest frame. This allows the physical variables, and hence, the emission and absorption coefficients and their changes along a ray, to be parametrised by the cosmological redshift only. The propagation of the radiation is parametrised by the redshift  $z$  which is divided into  $N_z$  discrete cells along each ray. In addition to the discretisation along the ray, another sampling in frequency on each  $z$ -grid is constructed to account for the changes in the line profile and the continuum along the ray. The sampling scheme has been constructed to optimise the efficiency in the line radiative transfer calculations. The design of the algorithm and its optimisation are described in Appendix A.

Solving the cosmological 21-cm line radiative transfer equation, Eqn. (25), requires (i) the specification of initial radiation background, and (ii) the determination of the continuum and the line transfer coefficients over a frequency range fully covering the line and the relevant underlying continuum in the local rest frame. For (i), the CMB provides the continuum radiation background that must be accounted for when considering the cosmological 21-cm line. If bright radio sources are present along some rays, their emission at and adjacent to the 21-cm line centre will be the dominant background radiation. As per (ii), the line transfer coefficients (Eqn. (13) and Eqn. (14)) can be computed when the line profile function  $\phi_\nu$  and the number densities of HI atoms  $n_{\text{HI}}$  in the two hyperfine states  $n_{\text{l}}$  and  $n_{\text{u}}$  at each location along the ray are known. Modelling of either  $n_{\text{l}}$  or  $n_{\text{u}}$  and  $n_{\text{HI}}$  in astrophysical environments involves detailed investigations of the spin-flip mechanisms at play and is beyond the scopes of this work. Here, a post-processing approach is adopted for

which, given an input model of these parameters, the line transfer coefficients can be computed and the (cosmological) 21-cm line radiative transfer calculations can be conducted to predict the observed spectra at individual lines-of-sight. For calculations in the cosmological context, the upper limit of  $n_{\text{HI}}$  is constrained by the baryonic number density and can be further combined with a spin temperature model  $T_s(z)$  to calculate  $n_l$  or  $n_u$ .

## 4.2 Code verification

A number of numerical tests are conducted to verify the implementation of the algorithm and the execution of the code for C21LRT calculations. Appendix B shows the set-up and the numerical results of two example tests that verify the ability of the code to correctly account for the cosmological expansion effects on the transport of continuum radiation. Below we summarise what these calculations reveal, in the context of the determination and interpretation of tomographic 21-cm spectra that would be observed, in addition to fulfilling their designs for code verification purposes.

Appendix B1 show the cosmological transport of the CMB radiation, as a continuum background, in a self-consistent manner as to the transfer of the 21-cm line. Machine floating point residuals are obtained, indicating the robustness of the C21LRT numerical scheme for scientific investigations building towards high-precision cosmological studies of reionisation, which would require calculations for cosmological radiative transfer of the 21-cm line in the presence of continuum from the Cosmic Dawn and the EoR, up to the present. Such a calculation will be presented in Section 5.

Appendix B2 shows the frequency shift, width compression (in the frequency space) and intensity suppression (due to Lorentz invariance) in cosmological radiative transfer. The compression of the line width is significant in the cosmological evolutionary context. For instance, the  $\text{FWHM}_\nu$  of a line created at  $z = 10$  would be reduced to a  $\text{FWHM}_\nu/(1+z) = \text{FWHM}_\nu/11$  when it is observed at  $z = 0$ . This width reduction is caused by the expansion of the Universe, and the line width is scaled by  $[(1+z)/(1+z_{\text{emi}})]$  (see Appendix B2 for details), which is the same as the scaling factor of the radiation frequency. This scaling will be cancelled out if  $\Delta\nu/\nu$  (where  $\Delta\nu$  is the line width) is used in an observational analysis. Interpretation of data using a theoretical model is an inverse process. Therefore, caution must be taken when using the line width in interpreting spectroscopic results associated with distant sources, and, in particular, the subtleties on cosmological expansion effects and on local physical processes that lead to the change in the line profile must be properly accounted for.

## 5 21-CM TOMOGRAPHY WITH C21LRT

With the validated ray-tracing code, here, the C21LRT equation is solved in representative cosmological settings from  $z_{\text{max}} = 35.37$  to the present epoch along a single ray, demonstrating the convolution of cosmological effects and radiative transfer effects when they are properly accounted for.

The diffuse gas suffusing the Universe (hereafter, referred to as the intergalactic medium (IGM) after the appearances of the first luminous structures) consist of two phases: (i) ionised (hereafter, referred to as H II, without losing generality) gas in bubbles embedded with luminous sources that supply the ionising photons, (ii) largely neutral IGM in regions outside the H II bubbles. Gas inside the H II bubbles with a strong radiation field is practically fully ionised, as recombination cannot keep up with ionisation. Gas in regions far

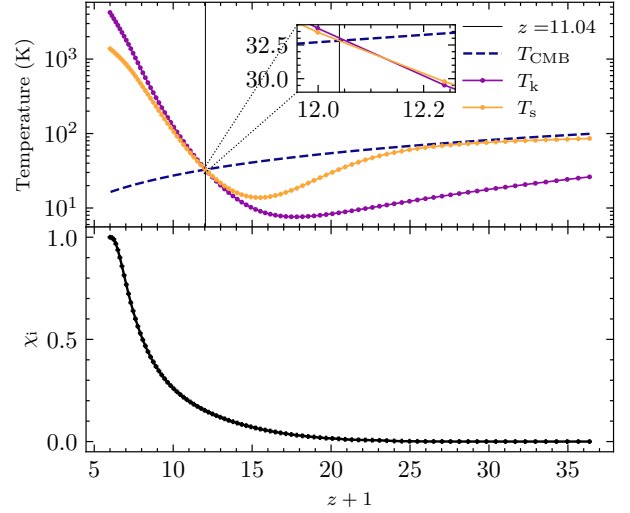


**Figure 1.** Input properties of HI gas into C21LRT code based on simulation result of 21CMFAST (Muñoz et al. 2022). The globally averaged kinematic gas temperature  $T_k$ , spin temperature of 21-cm line  $T_s$  and the CMB temperature  $T_{\text{CMB}}$  are plotted in the upper panel in purple, yellow and blue (dashed line), respectively. The globally averaged ionisation fraction of HI  $x_i$  is plotted in the bottom panel in black. The dots in the lines for  $T_k$ ,  $T_s$  and  $x_i$  are obtained from 21CMFAST simulation snapshots (Muñoz et al. 2022). To match the redshift resolution of our calculation in C21LRT code, we linearly interpolate these quantities between the maximum ( $z_{\text{max}} = 35.37$ ) and minimum redshifts ( $z_{\text{min}} = 5.0$ ). At  $z_{\text{transition}} = 11.04$ , the interpolated  $T_s$  equals to  $T_{\text{CMB}}$ . The zoomed-in patch shows the region near  $z_{\text{transition}}$ .

outside the bubbles would remain neutral. Ionised gas and neutral gas can co-exist in a transition region between the H II bubble and the ambient neutral medium. The ionisation state of the gas in these three regions can be described in terms of a parameter, the ionisation fraction  $x_i$ , with  $x_i = 0$  for neutral gas and  $x_i = 1$  for fully ionised gas.

In this demonstrative study, the detailed structures and the cosmological evolution of these three regions are not considered. Instead, the cosmological evolution of the ionisation state of the line-of-sight medium is parametrised by a volume-averaged value for the ionisation fraction, i.e.  $x_i(z)$ . In other words, the transfer of 21-cm line photons in the H II bubble, the neutral medium and the transition regions are not explicitly distinguished.

We adopt the globally averaged  $T_s(z)$  and  $x_i(z)$  from the ‘EOS 2021 all galaxies simulation’ result (which used the semi-analytical code 21CMFAST) (Muñoz et al. 2022) as the inputs of C21LRT calculations, as shown in Fig. 1. We also plot  $T_k$  and  $T_{\text{CMB}}$  in the upper panel for comparison. To match the redshift resolution of our calculation, we linearly interpolated  $T_s(z)$  and  $x_i(z)$  between the maximum ( $z_{\text{max}} = 35.37$ ) and minimum redshifts ( $z_{\text{min}} = 5.0$ )<sup>7</sup>. At  $z_{\text{transition}} = 11.04$ , the interpolated  $T_s$  equals  $T_{\text{CMB}}$ . For  $z < 5.0$ , we consider the remaining HI negligible for the global 21-cm signal. We

<sup>7</sup> The redshift limits are chosen because the simulated results are only available between  $z_{\text{max}}$  and  $z_{\text{min}}$ .

let  $x_i = 0$  and do not consider further modifications of the radiations due to HI at  $z < z_{\min}$ <sup>8</sup>.

In this study, we consider only CMB as the continuum radiation background. Other continuum radiative processes, such as thermal and non-thermal free-free processes and synchrotron radiation, are ignored. Then based on the input  $T_s(z)$ , we expect to see two regimes: one for absorption and one for emission. Between  $z_{\max}$  and  $z_{\text{transition}}$ , the competition between radiative coupling with the CMB and the collisional coupling leads to  $T_{\text{CMB}} \gtrsim T_s > T_k$ , and the 21-cm signal is in an absorption regime. Afterwards, the first luminous sources released UV radiation and X-rays which ionised and heated the HI gas. This ushered the Universe into the cosmological reionisation epoch. More importantly, the UV radiation would give rise to Ly $\alpha$  pumping process, and the hyperfine states of the HI gas were no longer determined solely by the thermal and collision coupling processes. The Ly $\alpha$  radiation boosted the relative populations of HI atoms in the upper (triplet) hyperfine state via the Wouthuysen-Field mechanism, while the heating by UV radiation and X-rays of the HI gas resulted in  $T_k > T_r$ . Hence the 21-cm signal is in an emission regime between  $z_{\text{transition}}$  and  $z_{\min}$ .

With  $x_i(z)$  specified, the amount of HI gas and the relative population of HI atoms in the two hyperfine states can be computed given a cosmological model, with the procedures described as follows. The density of hydrogen is approximately 75% of the baryon density by mass, i.e.  $\rho_{\text{H}} = 3\rho_{\text{b}}/4$ , and the remaining 25% is mainly contributed by helium, especially before the mass production of metals in stars. Assuming a two-species (H-He) description of the baryonic content, the cosmological number density of hydrogen is then

$$\begin{aligned} \bar{n}_{\text{H}}(z) &= (\Omega_{\text{b}}(z)/m_{\text{p}}) \rho_{\text{crit}} (1 - Y_{\text{He}}) \\ &\approx (\Omega_{\text{b},0}/m_{\text{p}}) (1+z)^3 \rho_{\text{crit}} (1 - Y_{\text{He}}) \\ &= \bar{n}_{\text{H},0} (1+z)^3. \end{aligned} \quad (36)$$

In the calculations, the mass fraction of helium is set to be  $Y_{\text{He}} = 1/4$ . The present baryonic density  $\rho_{\text{b},0} = 4.18977 \times 10^{-31} \text{ g cm}^{-3}$ , deduced from  $\Omega_{\text{b},0} = \rho_{\text{b},0}/\rho_{\text{crit}}$ , where  $\Omega_{\text{b},0} h^2 = 0.02230$  (Planck Collaboration XIII 2016),  $\rho_{\text{crit}} = 3H_0/(8\pi G) = 1.87882 \times 10^{-29} h^2 \text{ g cm}^{-3}$  (with  $h = 0.6774$ ), and hence, the present hydrogen number density  $\bar{n}_{\text{H},0} = 1.87745 \times 10^{-7} \text{ cm}^{-3}$ . It follows that

$$\bar{n}_{\text{HI}}(z) = \bar{n}_{\text{H}}(z) x_{\text{HI}}(z) = \bar{n}_{\text{H}}(z) (1 - x_i(z)). \quad (37)$$

For each ray traced in our calculations, the propagation of the radiation along the ray is stamped by the redshift  $z$ . The number density of the HI atoms in the lower (singlet) hyperfine state along one ray is given by

$$\begin{aligned} n_1(z) &= \frac{n_{\text{HI}}(z)}{1 + 3 \exp(-T_{\star}/T_s(z))} \approx \frac{n_{\text{HI}}(z)}{4 - 3(T_{\star}/T_s(z))} \\ &= \frac{\bar{n}_{\text{H}}(z) x_{\text{HI}}(z) (1 + \delta_{\text{b}}(z))}{4 - 3T_{\star}/T_s(z)}, \end{aligned} \quad (38)$$

for  $T_s \gg T_{\star}$ , where the baryonic matter overdensity is  $\delta_{\text{b}} \equiv (\rho_{\text{b}}/\bar{\rho}_{\text{b}} - 1)$ , with  $\bar{\rho}_{\text{b}}$  being the mean density. The corresponding

<sup>8</sup> After the completion of the cosmological reionisation, only the self-shielded surviving dense clumps of HI would contribute to the cosmological 21-cm line signals. The observational imprints caused by convolution of these dense HI structures in the post-reionisation era and the ionised bubbles developed in the EoR have not been thoroughly investigated. Although these complex issues will not be addressed in the demonstrative calculations here, they can be studied explicitly and their observational consequences can be quantified using the C21LRT formulation.

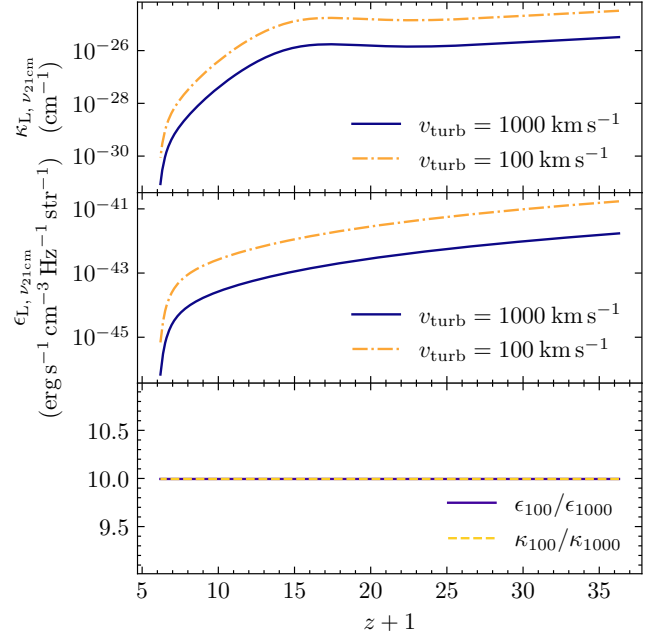


**Figure 2.** The absorption and emission coefficients ( $\kappa_{L,\nu 21\text{cm}}$  and  $\epsilon_{L,\nu 21\text{cm}}$ ) of 21-cm line at the frequency  $\nu = \nu_{21\text{cm}}$  evaluated in the comoving frame at  $z$ . Coefficients calculated with  $v_{\text{turb}} = 1000 \text{ km s}^{-1}$  and  $100 \text{ km s}^{-1}$  are plotted in the panel on top and in the middle, respectively. These coefficients are calculated within the C21LRT code and saved along with other results. The ratio of absorption and emission coefficients when adopting  $v_{\text{turb}} = 100 \text{ km s}^{-1}$  and  $1000 \text{ km s}^{-1}$  are plotted in the bottom panel, with solid purple line and dashed yellow line, respectively. Both their values are exactly 10 determined by the (normalised) line profile as discussed in Sec 3.2.2.

number density of the HI atoms in the upper (triplet) hyperfine state is given by  $n_{\text{u}}(z) = n_{\text{HI}}(z) - n_1(z)$ . Therefore,

$$n_{\text{u}}(z) \approx \frac{3 \bar{n}_{\text{H}}(z) x_{\text{HI}}(z) (1 + \delta_{\text{b}}(z)) (1 - T_{\star}/T_s(z))}{4 - 3T_{\star}/T_s(z)}. \quad (39)$$

The above parametrisation of the relative population of HI atoms in the two hyperfine states, ( $n_{\text{u}}/n_1$ ), using the spin temperature  $T_s$  has imposed a constant 3 : 1 ( $= g_{\text{u}} : g_1$ ) ratio for the relative populations<sup>9</sup>

With the properties of HI specified, we still need to specify the line profile of 21-cm line to determine the 21-cm radiative processes. Line broadening caused by thermal motion is insignificant in this demonstrative study<sup>10</sup>. The line broadening is, therefore, caused only by turbulent motion characterised by a root-mean-square velocity  $v_{\text{turb}}$ . Furthermore,  $v_{\text{turb}}$  is assumed to be uniform along the line-of-sight and constant through out one set of calculation. We do not consider the other types of relative velocities of the HI gas along line-of-sight and leave redshift space distortion effects to future studies.

<sup>9</sup> Although beyond the scope of this study, we note that this parametrisation will be invalid if there is a strong UV radiation field. The Ly $\alpha$  pumping will allow a higher number of HI atoms in the upper hyperfine state through the Wouthuysen-Field mechanism. In this situation, an additional local radiative transfer calculation will be required so to determine  $n_{\text{u}}$  and  $n_1$ .

<sup>10</sup> To match the broadening caused by  $v_{\text{turb}} = 10 \text{ km s}^{-1}$ , we need  $T_k = 6060.67 \text{ K}$ , which is already higher than expected  $T_k$  of HI as shown in Fig. 1.



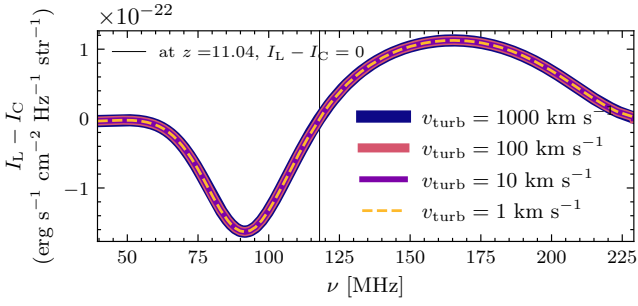


**Figure 3.** Spectra of 21-cm line at  $z = 0$  using the inputs from Fig. 1, with various assumed turbulent velocity. The spectra calculated with  $v_{\text{turb}} = 1000, 100, 10, 1 \text{ km s}^{-1}$  are plotted in blue (thickest, in the bottom layer), crimson, purple and yellow (thinnest, in the top layer, with dashed line). These lines are perfectly overlapped all over the plotted frequency range when inspected by eye, as expected (see detailed explanation in main text). The relative difference between these four scenarios is small (see Appendix A for details.). The intensity of 21-cm line (after subtracting CMB continuum) changes from negative to positive at  $\nu = 118.97 \text{ MHz}$ , which corresponds to  $z = 11.04$  where  $T_s = T_{\text{CMB}}$  in Fig. 1.

## 6 RESULTS AND DISCUSSION

### 6.1 Line transfer coefficients

At a given  $z$ , the variation of the transfer coefficients across the line frequency  $\nu$  follows the line profile function  $\phi_\nu$ . Fig. 2 shows the transfer coefficients of the HI hyperfine line (without a continuum) at the line centre, evaluated in the comoving  $z$  frames for the case with  $v_{\text{turb}} = 1000 \text{ km s}^{-1}$  and the comparison with the cases with  $v_{\text{turb}} = 100 \text{ km s}^{-1}$ . The emission and absorption coefficients at the line centre  $\kappa_{L,\nu 21\text{cm}}$  and  $\epsilon_{L,\nu 21\text{cm}}$  are proportional to  $1/v_{\text{turb}}$  as discussed in Sec 3.2.2, shown in the bottom panel. As the corresponding  $\text{FWHM}_\nu$  is relatively small compared to the entire frequency range in the 21-cm spectra at  $z = 0$ , even when we adopt  $v_{\text{turb}} = 1000 \text{ km s}^{-1}$ , and the 21-cm line profile is well resolved in frequency space, we do not expect the difference to show up in the 21-cm global spectra calculated with smooth HI properties in this paper. The differences due to different  $v_{\text{turb}}$  is significant when the properties of HI changes on scales comparable to or smaller than  $\text{FWHM}_\nu$ , as analysed in Wu et al. (2023).

### 6.2 Tomographic 21-cm Spectra

The radiative transfer of the 21-cm hyperfine line from  $z_{\text{max}}$  to  $z = 0$  (the present epoch) is solved using a ray-tracing approach with the input specified in Sec 5 (see Fig. 1), while adopting various turbulent velocities.

Spectra of 21-cm line at  $z = 0$  calculated with  $v_{\text{turb}} = 1000, 100, 10, 1 \text{ km s}^{-1}$  are shown in Fig. 3 with thicker lines corresponding to larger  $v_{\text{turb}}$  ( $v_{\text{turb}} = 1000 \text{ km s}^{-1}$  in blue with the thickest line in the bottom layer,  $v_{\text{turb}} = 100, 10 \text{ km s}^{-1}$  in crimson and purple,  $v_{\text{turb}} = 1 \text{ km s}^{-1}$  in yellow with thinnest dashed line in the top layer). These spectra are perfectly overlapped over the entire plotted frequency range when inspected by eye, as expected. Quantitatively, the relative difference between these four scenarios are small, on order of magnitudes of  $10^{-5} - 10^{-4}$  (see Appendix A for details). The intensity of 21-cm line (after subtracting CMB continuum) changes from negative to positive at  $\nu = 118.973 \text{ MHz}$ , which corresponds to  $z = 11.04$  where  $T_s = T_{\text{CMB}}$  in Fig. 1.

We track the development of the prominent spectral features and

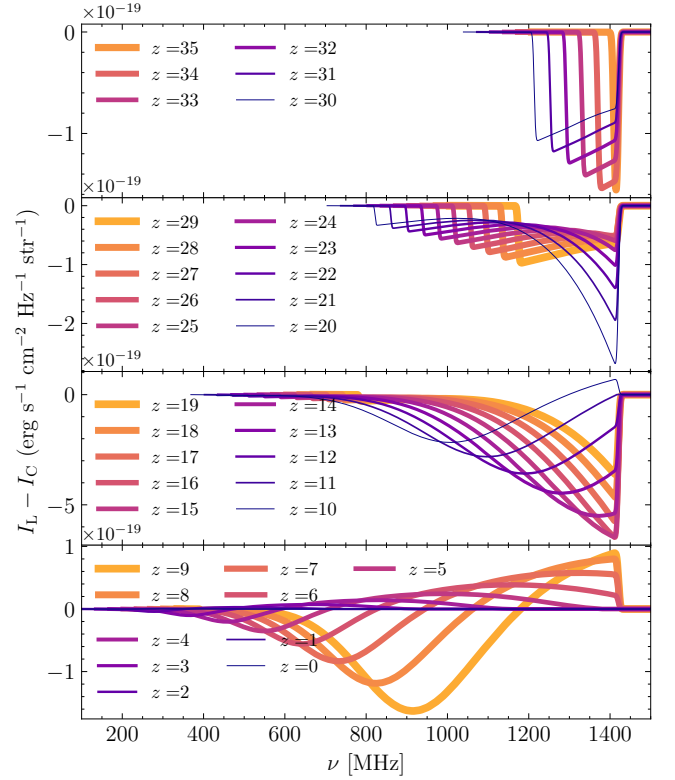


**Figure 4.** Spectra of the 21-cm line in the rest frames of  $z = 35, 34, \dots, 0$  when the C21LRT calculated has been carried out to the corresponding redshifts. In each panel, higher-redshift results are plotted with thicker lines. The spectrum corresponding to the highest and lowest redshift in a panel is coded in orange and purple, respectively. For all spectra, the y-value (specific intensity) collapses to 0 quickly near  $\nu_{21\text{cm}}$ . This is because the radiative transfer calculation has only been carried out to a certain redshift. In the rest frame of this redshift, the amount of emission blueward of  $\nu_{21\text{cm}}$  is negligible. Also, the strength of the signal is reduced from higher to lower redshift as the result of cosmological expansion. This effect is most noticeable in the bottom panel, where the spectra corresponding to the lowest redshift values have almost collapsed to 0 (see Fig. 3  $I_L - I_C \sim 10^{-22} \text{ erg s}^{-1} \text{ cm}^{-3} \text{ Hz}^{-1} \text{ str}^{-1}$  at  $z = 0$ ).

how they change in amplitude and shift in redshift space as the radiation propagated down to  $z = 0$ . We show spectra in the local rest frames at  $z = 35, 34, \dots, 0$  in Fig. 4. In each panel, higher redshift results are plotted with thicker lines. For example, in the top panel, the spectra corresponding to  $z = 35$  and  $z = 30$  are plotted with the thickest orange and thinnest purple lines, respectively. For all spectra, the y-value (intensity) collapses to 0 quickly near  $\nu_{21\text{cm}}$ . This is because the calculation has only been carried out to a certain redshift. In the rest frame of this redshift, the amount of emission blueward of  $\nu_{21\text{cm}}$  is negligible. The strength of the 21-cm signal is reduced from higher to lower redshift as the consequence of cosmological expansion. This effect is most noticeable in the bottom panel. The maximum negative intensity is  $I_L - I_C \sim 10^{-19} \text{ erg s}^{-1} \text{ cm}^{-3} \text{ Hz}^{-1} \text{ str}^{-1}$  for  $z = 9$ , which can be compared to the spectra in Fig. 3 where  $I_L - I_C \sim 10^{-22} \text{ erg s}^{-1} \text{ cm}^{-3} \text{ Hz}^{-1} \text{ str}^{-1}$  at  $z = 0$ .

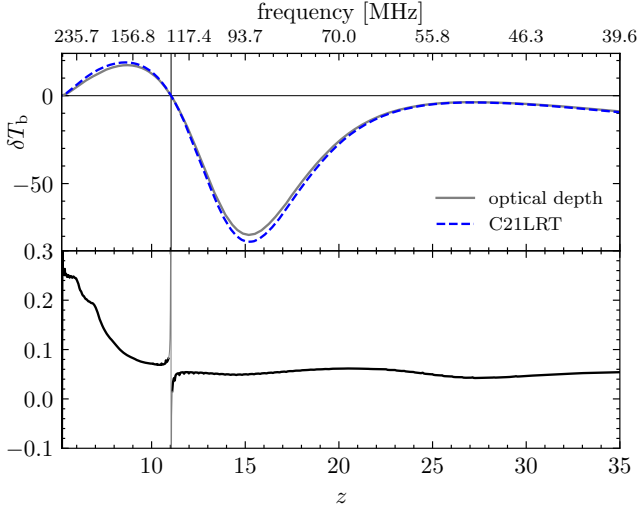


**Figure 5.** Comparing the results from C21LRT calculations and optical method on 21-cm differential brightness temperature  $\delta T_b$  - redshift  $z$  diagram. In the upper panel,  $\delta T_b$  calculated with C21LRT and optical depth parametrisation (Eqn. (40)) are plotted in blue dashed line and grey solid line, respectively. The relative difference  $\delta T_b \text{ C21LRT} / \delta T_b \text{ optical depth} - 1$  is plotted in the lower panel. The region around  $z_{\text{transition}} = 11.04$  is made less apparent intentionally because this is where  $\delta T_b$  is very close to zero near  $z_{\text{transition}}$  and the relative difference increases artificially. In the upper panel,  $z_{\text{transition}}$  and  $\delta T_b = 0$  are marked with thin black lines.

### 6.3 Compare C21LRT with the optical-depth parametrisation

Current calculations of 21-cm tomographic spectra often use the following expression:

$$\begin{aligned} \delta T_b &\approx \left( \frac{T_s - T_r}{1+z} \right) \tau_\nu \\ &\approx 27 x_{\text{HI}} (1 + \delta_b) \left( \frac{\Omega_b h^2}{0.023} \right) \left( \frac{0.15}{\Omega_m h^2} \right)^{1/2} \left( \frac{1+z}{10} \right)^{1/2} \\ &\quad \times \left( \frac{T_s - T_r}{T_s} \right) \left[ \frac{\partial_r v_r}{(1+z) H(z)} \right] \text{mK} \end{aligned} \quad (40)$$

(see Furlanetto et al. 2006; Pritchard & Loeb 2012; HERA Collaboration 2022). Here,  $T_r$  is the brightness temperature of the background radiation at the relevant frequency,  $x_{\text{HI}}$  is the neutral fraction of hydrogen,  $\delta_b$  is the fractional over-density in baryons, and  $\partial_r v_r$  specifies the gradient of proper velocity along the line-of-sight. The expression was derived in Furlanetto et al. (2006), where various approximations were taken to obtain such an analytical expression. Most importantly, they assumed that (i) HI gas is moving uniformly with the Hubble flow then used this assumption to skip distance integration (length of the HI gas) and frequency integration (frequency range defined by 21-cm line profile at a given distance)<sup>11</sup>. This essentially wipes out the contribution of variations in  $n_{\text{HI}}$  and  $T_s$  on small scales to the variations in the 21-cm signal.

The other minor approximations adopted while deriving Eqn. (40) were (ii) the values of the physical constants or quantities are truncated at only a few digits (e.g. the value of Einstein coefficient), (iii) stimulated emission is approximated in first order (of spin temperature  $T_s$ ), (iv) local thermodynamics equilibrium (LTE) is always

assumed (see Eqn. (20) and discussion in Sec 3.1), and (v) radiative transfer effects were assumed to be insignificant.

We calculated the 21-cm differential brightness temperature  $\delta T_b$  with Eqn. (40) and used the same inputs ( $x_i$  and  $T_s$ ) as well as cosmological parameters. The result is shown in Fig. 5 as indicated with the solid grey line in the upper panel. For comparison, the result obtained with C21LRT (the same in Fig. 3) is shown in the same figure with the blue dashed line. Their relative difference  $\delta T_b \text{ C21LRT} / \delta T_b \text{ optical depth} - 1$  is plotted in the lower panel. After verifying the differences caused by the minor approximations (ii)-(v) one by one, we found that they all leads to differences less than 1%. We conclude that the  $\geq 5\%$  level difference in the lower panel is caused by the major approximation (i), which is to invoke Hubble flow and skip distance and frequency integration. The relative difference seems to be evolving with redshift and increases quickly after  $z < 11$ . We therefore tested the discrepancy between Eqn. (40) and C21LRT with arbitrary  $T_s$ . We found that the relative difference always increases towards lower redshift regardless of the input  $T_s$ . We tentatively conclude that this is because the major approximation (which used the Hubble flow to skip integration) deviates more from actual distance and frequency integration calculations at lower redshift. We note that the  $\geq 5\%$  level relative difference already warrant more investigation and implies that we may derive a more accurate analytical expression with approximate distance and frequency integration.

In the context of 21-cm tomography, this approximation implies that the observed  $\delta T_b$  at  $z = 0$  at a specific frequency  $\nu_0$  is unambiguously connected to frequencies  $\nu|_z = \nu_0 (1+z)$  along the-line-sight in the redshift space (as in the ray-tracing shown in Fig. A2), with contribution weighted by the opacity appropriate for line-of-sight radiation field and media. The one-to-one connection between  $\nu_0$  and  $\nu|_z$  along the line-of-sight would break down, when there is a frequency spread in the 21-cm line, induced by local thermal and dynamical properties of the line-of-sight media. This frequency spread will not pose a very serious problem when the line is optically thin and when there is no convolution between the broadened 21-cm line and its neighbouring continuum in the radiative transfer, i.e. the expression in Eqn. (40) is applicable. However, in real situations, we usually have a 21-cm line broadened by the local dynamics, such as bulk motion and turbulence. The time (redshift) ordering and the frequency ordering become entangled. Because of the convolution in the radiative transfer processes, the line signal in the 21-cm spectrum at a particular frequency  $\nu(z)$  when observed at  $z = 0$  will not properly reflect the physical conditions of the Universe at redshift  $z$ .

Note also that the  $\geq 5\%$  level relative difference pertains to a simple scenario of a smooth (globally averaged) model of reionisation and that the radio continuum background is solely attributed to the CMB. A more substantial difference is anticipated when considering the heterogeneous aspects of reionisation. For example,  $n_{\text{HI}}$  and/or  $T_s$  may change drastically at the boundaries of ionised zones created by luminous sources. Predicting  $\delta T_b$  for these regions based on Eqn. (40) would create corresponding sharp changes in the 21-cm signal, while in reality 21-cm line is likely to be broadened and a sudden change in the HI gas properties does not necessarily lead to sharp changes in 21-cm spectra (see Wu et al. (2023)). Furthermore, we have not evaluated additional factors contributing to the continuum background, such as emissions from bright radio sources. The effects of absorption and emission of continuum along the line-of-sight could further complicate the interplay between the line-continuum interactions, which is further discussed in Appendix C. Evaluating the impacts of these factors on the spectra need to be done in relation to their specific contexts. Such an assessment, which extends beyond the scope

<sup>11</sup> An alternative derivation and detailed interpretations of Eqn. (40) can also be found in Pritchard & Loeb (2012).

of this paper, is planned for our future research. We intend to use the C21LRT formulation, which is constructed without making specific assumptions about the radiation background, ionisation sources, line-of-sight media, or the history of reionisation, to (i) study the impact of these physical factors on the spectra, (ii) predict not only the spectra but also power spectra of 21-cm signals for more realistic, patchy reionisation scenarios, and, as an inherent bonus of this approach, (iii) perform quantitative assessment of the accuracy of the common optical depth parametrisation method.

#### 6.4 Observational perspective

While only single-ray C21LRT calculations were presented along with a focused discussion on the cosmological radiative transfer effects and their implications on the global tomographic 21-cm signals that would be seen by the observer at  $z = 0$ , which are targeted by experiments such as EDGES (Bowman et al. 2018), LEDA (Price et al. 2018), SARAS (Singh et al. 2018), SCI-HI (Voytek et al. 2014) and Prizm (Phillip et al. 2019), employing multiple-ray (i.e. pencil beam or all sky) C21LRT calculations will yield cosmological 21-cm images or fluctuations maps. The C21LRT formulation is able to take the advantage of the vast resources in the sophisticated reionisation simulations through interfacing the C21LRT calculations with simulations via a post-processing approach, where simulation outputs that provide the redshift and spatial evolution of various 21-cm line related quantities (e.g. number density of HI, spin temperature, thermal history of the IGM) are sourced to compute the transfer coefficients and the C21LRT equations, and by adopting an appropriate ray-tracing algorithm to solve the transfer equations, to obtain high-fidelity 21-cm spectra templates. Statistical properties of the observables in these maps can then be determined (e.g. Watkinson & Pritchard 2014; Watkinson et al. 2017; Majumdar et al. 2018; Chen et al. 2019; Watkinson et al. 2019; Greig et al. 2022; Choudhury et al. 2022) for drawing physical interpretations of observations and understanding of the cosmological reionisation, such as by LOFAR (van Haarlem et al. 2013), MWA (Tingay et al. 2013), HERA (DeBoer et al. 2017) and SKA (Mellema et al. 2015; Koopmans et al. 2015).

## 7 CONCLUSION

The observed spectral properties of 21-cm line radiation associated with cosmological reionisation are modified by both cosmological and astrophysical processes that span broad ranges of length scales and time scales over cosmic time. A covariant formalism for cosmological radiative transfer of the 21-cm line was devised from the first principles, based on conservation of phase-space volume of the radiation and the conservation of photon number. In the formulation, the local radiation processes are included explicitly in terms of the absorption and emission coefficients of the line and the continuum, and the local line broadening in terms of a multiplicative line profile function in the line transfer coefficients.

From this covariant formulation, a C21LRT equation was derived assuming FLRW space-time. A ray-tracing algorithm is adopted for the numerical code to solve the C21LRT equation. The code takes full account of global effects associated with cosmological evolution, local effects on line broadening and frequency shifting and the convolution caused by line and continuum radiative transfer. The code is verified by a battery of numerical tests: including the cosmological transfer of CMB continuum, the transfer of a generic line in an expanding universe, and the transfer of a 21-cm line in the presence of absorption in structured media with differential rotational motions.

We present a set of demonstrative calculations and generate tomographic 21-cm spectra using the reionisation history based on (Muñoz et al. 2022). We showed how the 21-cm spectral signal developed and propagated throughout EoR in C21LRT. We adopted Gaussian 21-cm line profiles determined by turbulent velocities and found that these Gaussian line profiles cause negligible difference to the 21-cm signal spectra at  $z = 0$ . This is mainly because we used the globally averaged HI gas properties, which are smoothly varying with redshift.

Compared the spectrum at  $z = 0$  with that obtained by the optical depth parametrisation (Eqn.40, Pritchard & Loeb (2012)), we have found the discrepancy between the  $\delta T_b$  at the level of 5% for redshift  $z \sim 12$  or higher and of  $> 10\%$  for redshift smaller than  $z \sim 8$ .

The C21LRT formulation's independence from specific assumptions regarding radiation background, ionisation sources, line-of-sight media, reionisation history, and the 21-cm line profile, enhances its utility in accurately predicting 21-cm signals during reionisation. We have demonstrated that our C21LRT formulation can explicitly and self-consistently treat (i) time (redshift) and frequency ordering, (ii) line-continuum interactions in the presence of emission and absorption, and (iii) convolution of line and continuum radiative transfer with cosmological expansion. Within the confines of this paper, we have focused on applying the C21LRT calculation to a globally smooth reionisation model and considering a radio continuum background solely consisting of the CMB. Future research building on the C21LRT formulation will delve deeper into the heterogeneous nature of reionisation, exploring how it impacts the observed spectra in more intricate scenarios. For instance, in Wu et al. (2023), we have investigated the redshifted 21-cm imprints across ionised cavities in an expanding universe, accounting for factors such as differing ionised bubbles sizes at different redshifts, as well as the distortion of the apparent shape of the ionisation front due to the finite speed of light. Additionally, upcoming investigations will look into the impacts on the 21-cm spectra in scenarios where a continuum component, in addition to the CMB, is present, such as emissions from bright radio quasars and galaxies. These studies will also investigate the 21-cm signals, both in spectra and power spectra, considering the diverse, complex dynamics that occur during reionisation across different cosmic environments and redshifts. Quantitative comparison will be drawn against the optical depth parametrisation method that often resorts to restrictive assumptions and approximations for analytical tractability but overlooks line and continuum radiative transfer effects and small-scale variations in the neutral hydrogen density and the spin temperature, as discussed in Section 6.3. These research efforts underscore the importance of proper covariant radiative transfer for computing model 21-cm spectra for extracting meaningful information regarding the structural development of the Universe from the (all-sky) 21-cm tomographic data, from observations such as those by MWA, HERA and SKA.

## ACKNOWLEDGEMENTS

We thank Jonathan Pritchard, Jacqueline Hewitt, Adrian Liu, Jordan Mirocha, Emma Chapman, Catherine Watkinson, Geraint Harker, Girish Kulkarni, Suman Majumdar, for discussions on astrophysics of the Epoch of Reionisation and 21-cm tomography, Thomas Kitching on the cosmological and astrophysical aspects of this study, John Richard Bond and Juna Kollmeier on treatments of transport processes, and Ziri Younsi on numerical covariant radiative transfer. JYHC acknowledges the enriching discussions and knowledge exchange regarding the theoretical and observational facets of reioni-

sation at the forums of the Pan-Canadian CITA Reionisation Focus Group and the CMB+EoR Summer Workshop at McGill University. JYHC was supported by the Natural Sciences and Engineering Research Council of Canada (NSERC) [funding reference #CITA 490888-16] by a CITA Postdoctoral Fellowship, as well as the University of Toronto Faculty of Arts & Science Postdoctoral Fellowship with the Dunlap Institute for Astronomy & Astrophysics. The Dunlap Institute is funded through an endowment established by the David Dunlap family and the University of Toronto. QH was supported by UCL through an Overseas Research Scholarship and the UK STFC through a postgraduate research studentship. QH, KW and JDM acknowledge the support from the UCL Cosmoparticle Initiative. This work was partially supported by a UK STFC Consolidate Grant awarded to UCL-MSSL. This work had made use of NASA's Astrophysics Data System.

## DATA AVAILABILITY

The theoretical data generated in the course of this study are available from the lead author, upon reasonable request.

## REFERENCES

- AlOmar S. A., 2020, *Optik*, 203, 163919
- Bacon R., et al., 2021, *A&A*, 647, A107
- Barkana R., Loeb A., 2001, *Phys. Rep.*, 349, 125
- Bennett C. L., et al., 2013, *ApJS*, 208, 20
- Bezanson R. d van Dokkum P., Franx M., 2012, *ApJ*, 760, 62
- Bond J. R., Kofman L., Pogosyan D., 1996, *Nature*, 380, 603
- Bowman J. D., Rogers A. E. E., Monsalve R. A., Mozdzen T. J., Mahesh N., 2018, *Nature*, 555, 67
- Boyer W., Lynas-Gray A. E., 2014, *MNRAS*, 444, 2555
- Breysse P. C., et al., 2022, *ApJ*, 933, 188
- Carilli C. L., 2011, *ApJ*, 730, L30
- Carilli C. L., Gnedin N. Y., Owen F., 2002, *ApJ*, 577, 22
- Chan J. Y. H., 2020, PhD thesis, UCL (University College London), London, UK
- Chan J. Y. H., Wu K., On A. Y. L., Barnes D. J., McEwen J. D., Kitching T. D., 2019, *MNRAS*, 484, 1427
- Chang T. C., Gong Y., Santos M., Silva M. B., Aguirre J., Doré O., Pritchard J., 2015, in *Advancing Astrophysics with the Square Kilometre Array (AASKA14)*. p. 4 ([arXiv:1501.04654](https://arxiv.org/abs/1501.04654))
- Chen Z., Xu Y., Wang Y., Chen X., 2019, *ApJ*, 885, 23
- Choudhury M., Datta A., Majumdar S., 2022, *MNRAS*, 512, 5010
- Ciardì B., Inoue S., Mack K., Xu Y., Bernardi G., 2015, *Proc. Sci.*, p. 6
- Colless M., et al., 2003, arXiv e-prints, [pp astro-ph/0306581](https://arxiv.org/abs/astro-ph/0306581)
- Dayal P., et al., 2020, *MNRAS*, 495, 3065
- DeBoer D. R., et al., 2017, *PASP*, 129, 045001
- Einstein A., 1916, *Physikalische Gesellschaft Z&uuml;rich*, 18, 47
- Einstein A., 1917, *Physikalische Zeitschrift*, 18, 121
- Essen L., Donaldson R. W., Bangham M. J., Hope E. G., 1971, *Nature*, 229, 110
- Field G. B., 1958, *Proc. of the IRE*, 46, 240
- Field G. B., 1959, *ApJ*, 129, 551
- Fuerst S. V., Wu K., 2004, *A&A*, 424, 733
- Furlanetto S. R., 2006, *MNRAS*, 370, 1867
- Furlanetto S. R., 2016, *The 21-cm line as a probe of reionization*. Springer International Publishing, p. 247, [doi:10.1007/978-3-319-21957-8\\_9](https://doi.org/10.1007/978-3-319-21957-8_9)
- Furlanetto S. R., Lidz A., 2007, *ApJ*, 660, 1030
- Furlanetto S. R., Loeb A., 2002, *ApJ*, 579, 1
- Furlanetto S. R., Oh S. P., 2005, *MNRAS*, 363, 1031
- Furlanetto S. R., Oh S. P., Briggs F. H., 2006, *Phys. Rep.*, 433, 181
- Geil P. M., Mutch S. J., Poole G. B., Duffy A. R., Mesinger A., Wyithe J. S. B., 2017, *MNRAS*, 472, 1324
- Gnedin N. Y., 2000, *ApJ*, 535, 530
- Gnedin N. Y., Shaver P. A., 2004, *ApJ*, 608, 611
- Gong Y., Cooray A., Silva M. B., Santos M. G., Lubin P., 2011, *ApJ*, 728, L46
- Greig B., Ting Y.-S., Kaurov A. A., 2022, *MNRAS*,
- Guzzo L., et al., 2014, *A&A*, 566, A108
- HERA Collaboration 2022, *ApJ*, 924, 51
- Haiman Z., Holder G. P., 2003, *ApJ*, 595, 1
- Hellwig H., Vessot R., Levine M., Zitzewitz P., Allan D., Glaze D., 1970, *IEEE Trans. Instrum. Meas.*, 19, 200
- Hogan C. J., Rees M. J., 1979, *MNRAS*, 188, 791
- Huchra J. P., et al., 2012, *ApJS*, 199, 26
- Hummer D. G., Rybicki G. B., 1985, *ApJ*, 293, 258
- Iliev I. T., Mellema G., Pen U. L., Merz H., Shapiro P. R., Alvarez M. A., 2006, *MNRAS*, 369, 1625
- Kannan R., Garaldi E., Smith A., Pakmor R., Springel V., Vogelsberger M., Hernquist L., 2022, *MNRAS*, 511, 4005
- Koopmans L., et al., 2015, in *Advancing Astrophysics with the Square Kilometre Array (AASKA14)*. p. 1 ([arXiv:1505.07568](https://arxiv.org/abs/1505.07568)), [doi:10.22323/1.215.0001](https://doi.org/10.22323/1.215.0001)
- Koopmans L., et al., 2021, *Exp. Astron.*, pp 1641–1676
- Kulkarni G., Choudhury T. R., Puchwein E., Haehnelt M. G., 2017, *MNRAS*, 469, 4283
- Libeskind N. I., et al., 2018, *MNRAS*, 473, 1195
- Lidz A., Zahn O., Furlanetto S. R., McQuinn M., Hernquist L., Zaldarriaga M., 2009, *ApJ*, 690, 252
- Lidz A., Furlanetto S. R., Oh S. P., Aguirre J., Chang T.-C., Doré O., Pritchard J. R., 2011, *ApJ*, 741, 70
- Loeb A., Furlanetto S. R., 2013, *The first galaxies in the Universe*. Princeton University Press, Princeton, NJ
- Mack K. J., Wyithe J. S. B., 2012, *MNRAS*, 425, 2988
- Madau P., Meiksin A., Rees M. J., 1997, *ApJ*, 475, 429
- Majumdar S., Pritchard J. R., Mondal R., Watkinson C. A., Bharadwaj S., Mellema G., 2018, *MNRAS*, 476, 4007
- Mather J. C., et al., 1994, *ApJ*, 420, 439
- McQuinn M., Lidz A., Zahn O., Dutta S., Hernquist L., Zaldarriaga M., 2007, *MNRAS*, 377, 1043
- Mellema G., Koopmans L., Shukla H., Datta K. K., Mesinger A., Majumdar S., 2015, in *Advancing Astrophysics with the Square Kilometre Array (AASKA14)*. p. 10 ([arXiv:1501.04203](https://arxiv.org/abs/1501.04203))
- Mesinger A., 2016, *Understanding the Epoch of cosmic Reionization: challenges and progress*. Astrophysics and space science library Vol. 423, Springer International Publishing, [doi:10.1007/978-3-319-21957-8](https://doi.org/10.1007/978-3-319-21957-8)
- Mesinger A., Furlanetto S., Cen R., 2011, *MNRAS*, 411, 955
- Mihalas D., 1978, *Stellar atmospheres*. W H Freeman & Co
- Mohankumar N., Sen S., 2019, *J. Quant. Spectrosc. Radiative Transfer*, 224, 192
- Morales M. F., Wyithe J. S. B., 2010, *ARA&A*, 48, 127
- Muñoz J. B., Qin Y., Mesinger A., Murray S. G., Greig B., Mason C., 2022, *MNRAS*, 511, 3657
- Nusser A., 2005, *MNRAS*, 359, 183
- Peacock J. A., 1999, *Cosmological physics*. Cambridge astrophysics, Cambridge University Press, Cambridge, <https://books.google.co.uk/books?id=t80-yy1U0j0C>
- Penzias A. A., Wilson R. W., 1965, *ApJ*, 142, 419
- Philip L., et al., 2019, *Journal of Astronomical Instrumentation*, 8, 1950004
- Planck Collaboration XIII 2016, *A&A*, 594, A13
- Planck Collaboration XVI 2014, *A&A*, 571, A16
- Price D. C., et al., 2018, *MNRAS*, 478, 4193
- Pritchard J. R., Loeb A., 2012, *Rep. Prog. Phys.*, 75, 086901
- Rien van de Weygaert Sergei Shandarin Enn Saar Jaan Einasto eds, 2016, *The Zeldovich Universe: Genesis and Growth of the Cosmic Web* Vol. 308, [doi:10.1017/S174392131601098X](https://doi.org/10.1017/S174392131601098X).
- Robertson B. E., Ellis R. S., Dunlop J. S., McLure R. J., Stark D. P., 2010, *Nature*, 468, 49
- Rutten R. J., 2003, *Radiative transfer in stellar atmospheres*. Sterrekundig Instituut Utrecht
- Rybicki G. B., Hummer D. G., 1978, *ApJ*, 219, 654

- Santos M. G., Amblard A., Pritchard J., Trac H., Cen R., Cooray A., 2008, *ApJ*, 689, 1
- Santos M. G., Ferramacho L., Silva M. B., Amblard A., Cooray A., 2010, *MNRAS*, 406, 2421
- Schreier F., 1992, *J. Quant. Spectrosc. Radiative Transfer*, 48, 743
- Scott D., Rees M. J., 1990, *MNRAS*, 247, 510
- Shin M.-S., Trac H., Cen R., 2008, *ApJ*, 681, 756
- Silva M. B., Santos M. G., Gong Y., Cooray A., Bock J., 2013, *ApJ*, 763, 132
- Silva M. B., et al., 2021, *Experimental Astronomy*, 51, 1593
- Singh S., Subrahmanyan R., Shankar N. U., Rao M. S., Girish B. S., Raghunathan A., Somashekar R., Srivani K. S., 2018, *Experimental Astronomy*, 45, 269
- Smoot G. F., et al., 1992, *ApJ*, 396, L1
- Spergel D. N., et al., 2003, *ApJS*, 148, 175
- Struble M. F., Rood H. J., 1999, *ApJS*, 125, 35
- Subramanian K., Padmanabhan T., 1993, *MNRAS*, 265, 101
- Sunyaev R. A., Zeldovich I. B., 1975, *MNRAS*, 171, 375
- Tegmark M., et al., 2004, *ApJ*, 606, 702
- Tingay S. J., et al., 2013, *Publ. Astron. Soc. Australia*, 30, e007
- Tucker H. W., 1977, *Radiation processes in astrophysics*. The MIT Press - Cambridge, MA, London
- Vernstrom T., Gaensler B. M., Vacca V., Farnes J. S., Haverkorn M., O’Sullivan S. P., 2018, *MNRAS*, 475, 1736
- Visbal E., Loeb A., 2010, *J. Cosmology Astropart. Phys.*, 2010, 016
- Voytek T. C., Natarajan A., Jáuregui García J. M., Peterson J. B., López-Cruz O., 2014, *ApJ*, 782, L9
- Watkinson C. A., Pritchard J. R., 2014, *MNRAS*, 443, 3090
- Watkinson C. A., Majumdar S., Pritchard J. R., Mondal R., 2017, *MNRAS*, 472, 2436
- Watkinson C. A., Giri S. K., Ross H. E., Dixon K. L., Iliev I. T., Mellema G., Pritchard J. R., 2019, *MNRAS*, 482, 2653
- White S. D. M., Frenk C. S., Davis M., Efstathiou G., 1987, *ApJ*, 313, 505
- Willott C. J., Rawlings S., Blundell K. M., Lacy M., 1998, *MNRAS*, 300, 625
- Wouthuysen S. A., 1952, *AJ*, 57, 31
- Wu K., Soria R., Hunstead R. W., Johnston H. M., 2001, *MNRAS*, 320, 177
- Wu K., Han Q., Chan J. Y. H., 2023, *MNRAS*, submitted
- Wyithe J. S. B., Loeb A., 2008, *MNRAS*, 383, 606
- Xu Y., Chen X., Fan Z., Trac H., Cen R., 2009, *ApJ*, 704, 1396
- Younsi Z., Wu K., Fuerst S. V., 2012, *A&A*, 545, A13
- Zaldarriaga M., Furlanetto S. R., Hernquist L., 2004, *ApJ*, 608, 622
- de Lapparent V., Geller M. J., Huchra J. P., 1986, *ApJ*, 302, L1
- van Haarlem M. P., et al., 2013, *A&A*, 556, A2
- van de Weygaert R., Schaap W., 2009, *The Cosmic Web: Geometric Analysis*. Springer, pp 291–413, doi:10.1007/978-3-540-44767-2\_11

## APPENDIX A: CODE CONVERGENCE AND OPTIMISATION

### A1 Optimisation of redshift and frequency grids

In logarithmic space, Eqn. (26) for the ray-tracing becomes

$$\log \nu_{z'} - \log \nu_z = \log(1+z') - \log(1+z). \quad (\text{A1})$$

Consider the intervals  $\Delta_{\log \nu} \equiv \log \nu_{z'} - \log \nu_z$ , and  $\Delta_{\log(1+z)} \equiv \log(1+z') - \log(1+z)$ . Then, Eqn. (A1) may be expressed as

$$\Delta_{\log \nu} = \Delta_{\log(1+z)}. \quad (\text{A2})$$

The computational grid is specified by the coordinates  $(j, k)$ , where the index “ $k$ ” runs through the redshift and the index “ $j$ ” through the radiation frequency. For a uniform sampling in  $\log(1+z)$ , through the index “ $k$ ”, and in  $\log \nu$ , through the index “ $j$ ”,  $\Delta_{\log \nu} = \Delta_{\log(1+z)} = C$ , where  $C$  is a positive constant. This gives a  $(j, k)$  lattice, and the ray tracing over cosmic time with a diagonal shift in the lattice (see Fig. A1). The sampling in  $\Delta_{\log \nu} = \Delta_{\log(1+z)} = C$  across the redshift is implemented such that

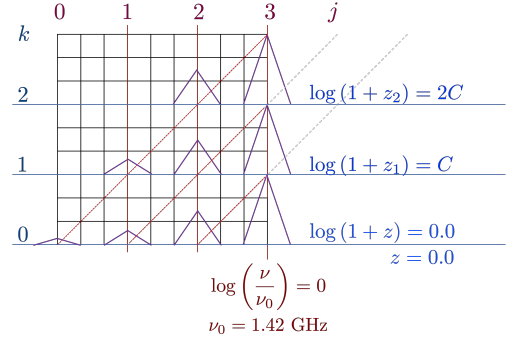


**Figure A1.** An illustration of a two-dimensional C21LRT square computational grid. The grid runs through the indices “ $k$ ” (for redshift) and “ $j$ ” (for frequency). Equal uniform samplings in  $\log(1+z)$ , through the index “ $k$ ”, and in  $\log \nu$ , through the index “ $j$ ” are adopted. The propagation of a ray is a diagonal shift in the computational grid coordinates  $(j, k)$ . The C21LRT calculations are performed along the rays as those indicated by the red dotted lines.

the line is sufficiently resolved to reveal the relevant physics of interest. Generally, the physical conditions evolve over the redshift on a slower rate than the line profile along the ray. For an appropriately chosen sampling in the frequency, a less dense sampling in the redshift will be sufficient in most of the situations. An optimal scheme with  $\Delta_{\log(1+z)} = C_1$  in the redshift sampling and  $\Delta_{\log \nu} = C_2$  in the frequency sampling, where  $C_1$  and  $C_2$  are positive constants, and their ratio  $C_1/C_2$  is set to be a fixed positive integer  $S$ , is adopted in the ray-tracing for the C21LRT calculations. The rectangular grid for the ray-tracing is illustrated in Fig. A2.

The ray is traced along the same  $j$  over a descending  $k$  (from a high redshift  $z_k$  to  $z_0 = 0$  at  $k = 0$ ). Along the ray, each grid point  $(j, k)$  has a uniquely assigned redshift, given by  $z_k = 10^{k \Delta_{\log(1+z)}} - 1$ , where  $\Delta_{\log(1+z)} = C_1 = [\log(1+z_{\max}) - \log(1+z_0)]/N_z$ . Also, a specific frequency is assigned to it, satisfying the rectangular grid specification as described above. At  $k = 0$ ,  $z_0 = z_{\text{obs}} = 0$ , and  $\nu(j, 0)$  is specified by the frequency from  $\nu_{\max}$  to  $\nu_{\min}$ , with the interval (resolution)  $\Delta_{\log(\nu)}|_{z_0} = [\log \nu_{\max} - \log \nu_{\min}]/N_j|_{z_0} = C_2$ . The radiation frequencies at higher redshifts are assigned by  $\nu(j, k)|_{z_k} = \nu(j, 0) \times (1+z_k)$ , satisfying Eqn. (A1). The frequency interval at each  $k$  is different. It scales by  $(1+z_k)$  with respect to that at  $z_0 = 0$ , with a coarser frequency interval at a higher  $z_k$ . The assignment of the frequency and the redshift to the computational grids are illustrated in Fig. A2. The constant integer ratio  $[\Delta_{\log(1+z)}/\Delta_{\log \nu}] = C_1/C_2 = S$  governs a constant shift in the  $j$  index of where  $\nu_{21\text{cm}}$  lies (denoted by  $\text{ind}_{21\text{cm}}$ ) at each  $z_k$ . If at  $k = 0$ ,  $\text{ind}_{21\text{cm}} = 0$  by a choice (i.e.  $\nu(0, 0) = \nu_{21\text{cm}}$ ), then, for  $k \geq 1$ ,  $\text{ind}_{21\text{cm}}|_{z_k} = -kS$ . Local 21-cm emission and absorption at all redshifts can, therefore, be tracked.

The algorithm can be optimised to increase computational efficiency. For instance, in certain post-reionisation epochs, where foreground effects are insignificant (i.e. absence of significant foreground absorption, emission, and line-continuum interaction), the radiative transfer of the 21-cm line can be performed simply by passing on the invariant specific intensity along the same  $j$  index as the index  $k$  descends to zero in the computational lattice. The local comoving specific intensity in the observer frame is calculated directly from invariant specific intensity.

The computational efficiency can further be boosted by an OpenMP parallelisation of the C21LRT code, when evaluating the frequency range (over the index  $j$ ) at each redshift (at a given  $k$ ). Consistent results are obtained using the OpenMP parallelised code as those obtained by the serial execution in all code verification tests.

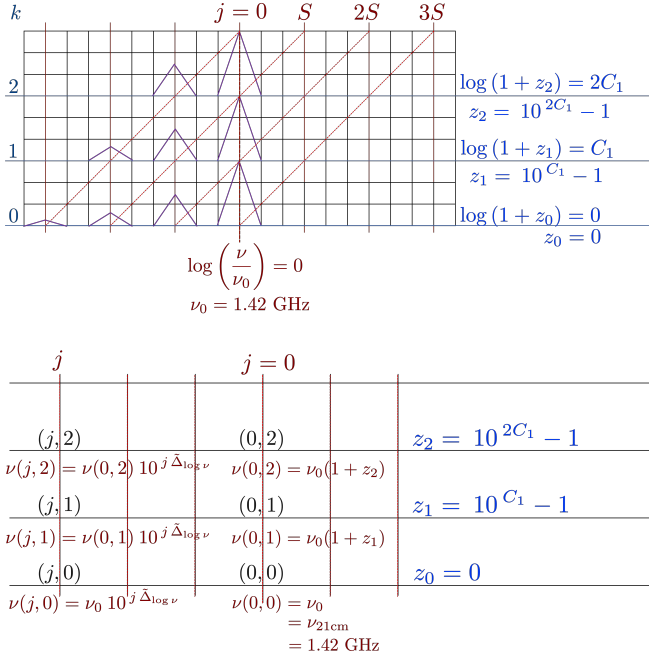


**Figure A2.** An illustration of the two-dimensional C21LRT rectangular computational grid (top panel), where frequency can be “reallocated” to each grid point (shown in the bottom panel). A uniform sampling is adopted in both  $\log(1+z)$  and  $\log \nu$ . The propagation of rays over cosmological redshift, represented by the red dotted lines in the top panel, corresponds to the tracing of the rays through the index “ $k$ ” with fixed “ $j$ ” in the lattice in the bottom panel.

## A2 Resolutions and convergence

The resolutions used in our code are constrained by two main aspects, which are to resolve the 21-cm line profile locally and preserve the line feature during radiative transfer from higher to lower redshift.

The frequency grid is set to resolve the local 21-cm profile at all redshifts where  $n_{\text{HI}}$  is positive. The redshift grid is set to ensure that there is enough overlap between the blue wing (higher frequency end) of the line profile in a given redshift cell ( $z = z_2$ ) and the red wing (lower frequency end) of the next lower redshift cell ( $z = z_1 < z_2$ ). The resolutions we adopted for the calculations in this paper are listed in Table A1.

As explained in Sec 3.2.2, the line profiles determined with  $v_{\text{turb}}$  in this paper only act as a redistribution of the emission or absorption over a frequency scale which is much smaller than the frequency range of the presented spectra. The 21-cm spectra calculated with various line widths are expected to be almost identical. We therefore present the relative differences for  $I_L - I_C$  when adopting various turbulent velocities in Table A2. We note that the absolute value of  $I_L - I_C$  can be very close to 0 at some frequencies (redshifts) ranges, including (i) at the beginning  $z = z_{\text{max}}$  and the end  $z = z_{\text{min}}$  of the radiative transfer calculation before conversion to the present-day values seen by an observer at  $z = 0$ , and (ii) at  $z \approx 11.04$  where the 21-cm signal changes from absorption to emission. When calculating the relative difference, we remove these frequencies (redshifts) ranges where the signal is too close to 0. In these ranges, the relative differences are about 0.5 to 1.3.

Although the 21-cm spectra is usually presented in  $I_L - I_C$ -frequency diagrams. The quantity that is calculated and propagated is  $I_L$ . We therefore also show the difference in  $I_L$  when adopting various turbulent velocities are listed in Table A3.

**Table A1.** The frequency and redshifts resolutions adopted for the calculations in this paper. The frequency resolution is set to resolve the 21-cm line profile in frequency space at all relevant redshift points. The redshift resolution is set to preserve 21-cm spectral features during radiative transfer from the highest relevant redshift  $z = z_{\text{max}}$  to  $z = 0$ .

$v_{\text{turb}}(\text{km s}^{-1})$	1000	100	10	1
$\Delta_{\log(1+z)}$	$1 \times 10^{-4}$	$1 \times 10^{-4}$	$1 \times 10^{-5}$	$1 \times 10^{-6}$
$\Delta_{\log \nu}$	$1 \times 10^{-5}$	$1 \times 10^{-5}$	$1 \times 10^{-5}$	$1 \times 10^{-6}$

**Table A2.** Relative difference in 21-cm line intensity ( $I = I_L - I_C$ ) between scenarios with different turbulent velocity  $v_{\text{turb}}$ . The relative difference is defined as, e.g.  $|I(v_{\text{turb}} = 100 \text{ km s}^{-1})/I(v_{\text{turb}} = 1000 \text{ km s}^{-1}) - 1|$  averaged over the frequency range presented in Fig. 3 as determined by  $z_{\text{max}}$  and  $z_{\text{min}}$ .

Relative dif- ference of ( $I = I_L - I_C$ )	$v_{\text{turb}}=1000$ $\text{km s}^{-1}$	$v_{\text{turb}}=100$ $\text{km s}^{-1}$	$v_{\text{turb}}=10 \text{ km s}^{-1}$
$v_{\text{turb}}=100$ $\text{km s}^{-1}$	$2.78 \times 10^{-4}$	-	-
$v_{\text{turb}}=10$ $\text{km s}^{-1}$	$3.46 \times 10^{-4}$	$1.56 \times 10^{-4}$	-
$v_{\text{turb}}=1$ $\text{km s}^{-1}$	$3.57 \times 10^{-4}$	$1.71 \times 10^{-4}$	$1.55 \times 10^{-5}$

**Table A3.** Relative difference in 21-cm line intensity ( $I = I_L$ ) between scenarios with different turbulent velocity  $v_{\text{turb}}$ . The relative difference is defined as, e.g.  $|I(v_{\text{turb}} = 100 \text{ km s}^{-1})/I(v_{\text{turb}} = 1000 \text{ km s}^{-1}) - 1|$  averaged over the frequency range presented in Fig. 3 as determined by  $z_{\text{max}}$  and  $z_{\text{min}}$ .

Relative dif- ference of ( $I = I_L$ )	$v_{\text{turb}}=1000$ $\text{km s}^{-1}$	$v_{\text{turb}}=100$ $\text{km s}^{-1}$	$v_{\text{turb}}=10 \text{ km s}^{-1}$
$v_{\text{turb}}=100$ $\text{km s}^{-1}$	$1.88 \times 10^{-6}$	-	-
$v_{\text{turb}}=10$ $\text{km s}^{-1}$	$2.49 \times 10^{-6}$	$1.11 \times 10^{-6}$	-
$v_{\text{turb}}=1$ $\text{km s}^{-1}$	$2.58 \times 10^{-6}$	$1.22 \times 10^{-6}$	$1.11 \times 10^{-7}$

## APPENDIX B: CODE VERIFICATION

### B1 Continuum radiative transfer

This test is to verify that the effect of cosmological expansion is properly account for in the absence of emission and absorption. The CMB has a blackbody spectrum, described by a Planck function with a single parameter, a thermal temperature. Its properties is well established observationally, and so it is chosen as a our test continuum.

#### B1.1 Set-up

A ray is traced from  $z_{\text{emi}} = 35.0$  to  $z = 0$ , with an initial specific intensity  $I_{\nu}|_{z_{\text{emi}}} = B_{\nu}(T_{\text{CMB}}|_{z_{\text{emi}}})$ . Without absorption and emission, the spectral evolution of the CMB is determined by the cosmological expansion only and can be parametrised by the redshift  $z$ . The CMB temperature scales with  $z$  as  $T_{\text{CMB}}(z)/(1+z) = T_{\text{CMB},0}$  in the FLRW universe, where  $T_{\text{CMB},0} = 2.73 \text{ K}$  at the current epoch (Spergel et al. 2003; Planck Collaboration XVI 2014).

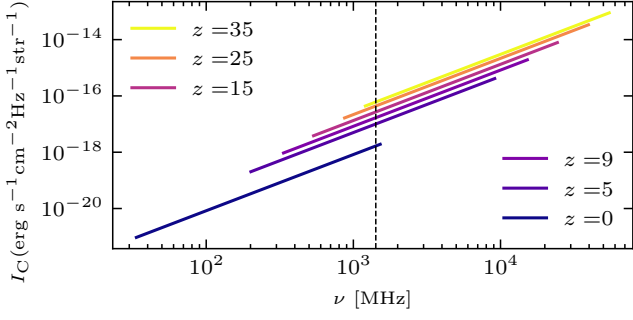


**Figure B1.** The transfer of the CMB from high to redshifts (in log-log representation). The frequency of hyperfine 21-cm transition of HI in the local rest frame, is marked with the vertical black dashed line.

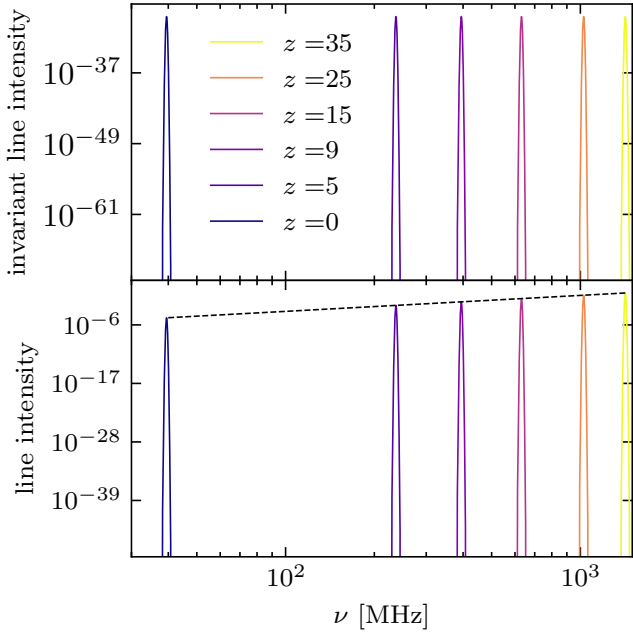


**Figure B2.** The computed invariant line intensity  $I_\nu$  (first panel, in units of  $\text{erg s}^{-1} \text{cm}^{-2} \text{Hz}^{-4} \text{str}^{-1}$ ) and line intensity  $I_\nu$  (second panel, in units of  $\text{erg s}^{-1} \text{cm}^{-2} \text{Hz}^{-1} \text{str}^{-1}$ ) against  $\nu$  in log-log scales, in an expanding universe without a line-of-sight medium and an external radiation field. The results show that  $I_\nu$  remains constant over redshift  $z$ ,  $I_\nu$  scales with  $[(1+z)/(1+z_{\text{emi}})]^3$ , and the line shape is preserved in the  $\log \nu$  space, all agreeing with the predictions of the analytical calculations.

### B1.2 Results

Fig. B1 shows the resulting CMB spectra at different cosmological epochs. The discrepancy between the computed and observed CMB spectra at  $z = 0$  is smaller than 1 part in  $10^{14}$  (i.e., comparable with machine floating-point precision).

## B2 Line radiative transfer

This test is to verify correct frequency shifting, broadening and Lorentz-invariance-induced suppression of intensity when the line is covariantly transported across the redshift space, in the absence of absorption and emission, via ray-tracing.

### B2.1 Set-up

The line propagates down in the redshift space from  $z_{\text{emi}} = 35.0$  to  $z = 0$ . The frequency shift of the line as it propagates is governed by a  $[(1+z)/(1+z_{\text{emi}})]$  factor (cf. Eqn. (26)), and this frequency shift has several consequences. (i) Without absorption and emission,  $I_\nu (= I_\nu/\nu^3)$  of the line is invariant in a covariant radiative transfer. The comoving specific intensity of the line  $I_\nu$  will therefore decrease accordingly, following  $[(1+z)/(1+z_{\text{emi}})]^3$ . (ii) The line width, expressed as a frequency spread, will be squeezed<sup>12</sup> (as opposed to the stretch when the line width is expressed as a wavelength spread) by a factor of  $[(1+z)/(1+z_{\text{emi}})]$ . The line width when expressed as velocity spread, however, remains unchanged. (iii) The line shape is distorted when it is expressed in terms of  $\nu$ , but preserves when it is expressed in terms of  $\log \nu$ .

We considered a line, which has a gaussian profile initially at  $z_{\text{emi}} = 35.0$  and is centred at  $\nu = 1.42 \text{ GHz} = \nu_{21\text{cm}}$ . It has a width  $\Delta\nu_{\text{D}} = 4.738 \text{ MHz}$ , corresponding to a velocity dispersion<sup>13</sup> of  $\Delta v = 1000 \text{ km s}^{-1}$ . The initial value of the peak specific intensity of the line is set to be  $I_\nu = 1.0 \text{ erg s}^{-1} \text{cm}^{-2} \text{Hz}^{-1} \text{str}^{-1}$  (in the local rest frame) at  $z_{\text{emi}} = 35.0$ .

### B2.2 Results

Fig. B2 shows the profiles of the line, in invariant specific intensity  $I_\nu$  (in units of  $\text{erg s}^{-1} \text{cm}^{-2} \text{Hz}^{-4} \text{str}^{-1}$ ) and comoving specific intensity  $I_\nu$  (in units of  $\text{erg s}^{-1} \text{cm}^{-2} \text{Hz}^{-1} \text{str}^{-1}$ ), at selected redshifts. As shown, the invariant specific intensity remains constant (in the top panel) but the specific intensity decreases (with a trend indicated by the dashed straight line in the bottom panel) as the line propagates from the high to low redshifts. The shape of the line is preserved in the  $\log \nu$  representation. These are the same as expected from theoretical consideration. The residuals of  $I_\nu$  and  $\nu$ , which are calculated by subtracting the ratio of the computed values to their corresponding analytical values by unity, attain a level below  $10^{-14}$ , reaching machine floating-point precision. The variations of the line

<sup>12</sup> Cosmological redshift  $z$  is defined as

$$(1+z_{\text{emi}}) \equiv \frac{\lambda_{\text{obs}}}{\lambda_{\text{emi}}} = \frac{\nu_{\text{emi}}}{\nu_{\text{obs}}},$$

with a rest-frame observer at  $z_{\text{obs}} = 0$ . This gives

$$(1+z_{\text{emi}}) = \frac{\nu_{\text{emi}} + \delta\nu_{\text{emi}}}{\nu_{\text{obs}} + \delta\nu_{\text{obs}}} = \frac{\nu_{\text{emi}}}{\nu_{\text{obs}}} \left[ \frac{1 + (\delta\nu_{\text{emi}}/\nu_{\text{emi}})}{1 + (\delta\nu_{\text{obs}}/\nu_{\text{obs}})} \right],$$

where  $\delta\nu_{\text{emi}}$  is a frequency displacement from  $\nu_{\text{emi}}$ , and  $\delta\nu_{\text{obs}}$  is the corresponding frequency displacement from  $\nu_{\text{obs}}$  measured by the observer. It follows from the two expressions that

$$\frac{\delta\nu_{\text{emi}}}{\nu_{\text{emi}}} = \frac{\delta\nu_{\text{obs}}}{\nu_{\text{obs}}},$$

which implies that

$$\frac{\delta\nu_{\text{obs}}}{\delta\nu_{\text{emi}}} = \frac{\nu_{\text{obs}}}{\nu_{\text{emi}}} = \frac{1}{(1+z_{\text{emi}})}.$$

If  $\delta\nu_{\text{emi}}$  is the marker of the width of a line, centred at  $\nu_{\text{emi}}$ , emitted from  $z_{\text{emi}}$ , the width of the line will reduce when measured by the observer in its local reference frame (for  $z_{\text{emi}} > z_{\text{obs}} = 0$  in an expanding Universe).

<sup>13</sup> The velocity dispersion of galaxies inside massive galaxy clusters (e.g. the Coma cluster Struble & Rood 1999) could have velocity dispersion  $\Delta v \approx 1000 \text{ km s}^{-1}$ . A large value of  $\Delta v (= 1000 \text{ km s}^{-1})$  is therefore selected to verify that the code has the dynamical range to handle this extreme level of line broadening. The velocity dispersion caused by the differential motions within a galaxy is smaller, generally in the range  $\Delta v \sim 100 - 400 \text{ km s}^{-1}$  (see e.g. Bezanson & Franx 2012). This gives rise to a frequency spread of  $\Delta\nu_{\text{D}} = 0.474 - 1.89 \text{ MHz}$ .

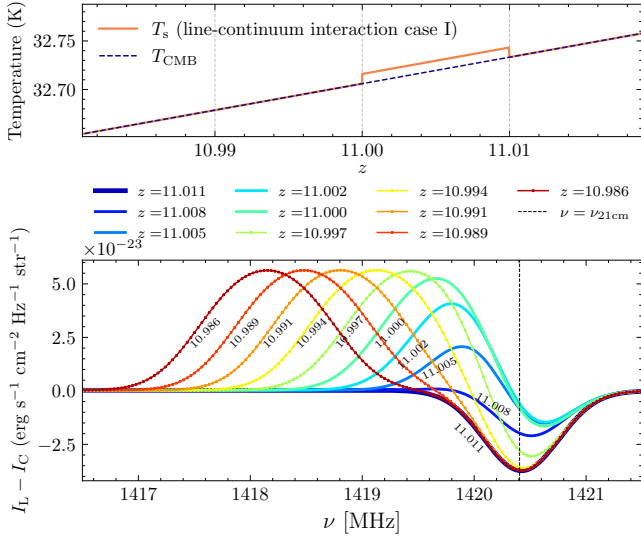


**Figure B3.** Line continuum interaction case I. The top panel shows the input spin temperature for our line continuum interaction calculation. The HI density is still the same as in Fig. 1. The spin temperature  $T_s$  is set to be  $0.01$  K higher than  $T_{\text{CMB}}$  between  $z = 11.00$  and  $z = 11.01$ , and  $T_s = T_{\text{CMB}}$  at  $z > 11.01$  or  $z < 11.00$ . The turbulent velocity  $v_{\text{turb}}$  is set to be  $100$  km s $^{-1}$ . This would generate a narrow emission signal in the local rest frame. The bottom panel shows the spectra calculated with C21LRT in the local rest frame of over redshift  $z = 10.986 - 11.011$ . See main text for the how line continuum interaction shaped these spectra.

frequency, characterised by the full-width-half-maxima,  $\text{FWHM}_\nu$  in frequency and  $\text{FWHM}_v$  in velocity, also agree with the analytical values at a level of  $10^{-13}$ .

### APPENDIX C: LINE-CONTINUUM INTERACTION

Using the optical depth parametrisation also ignores the convolution of the line transfer and the continuum transfer (see Tucker 1977; Hummer & Rybicki 1985; Wu et al. 2001), which are characterised by different opacities. For radiative transfer through structures with a non-uniform line-of-sight velocity field, the convolution of the line transfer and the continuum transfer can give rise to complex spectra (see Mihalas 1978; Rybicki & Hummer 1978; Hummer & Rybicki 1985). The line-continuum interaction also convolves with cosmological evolution (the time and frequency ordering mentioned in Sec 6.3). To illustrate how all of these effect are naturally taken into consideration within C21LRT calculations, we present two cases of 21-cm line and CMB continuum interaction, one exhibiting an emission line signal and one with absorption line signal.

To create an emission 21-cm signal, we set the spin temperature as  $T_s = T_{\text{CMB}} + 0.01$  K in a narrow redshift range (from  $z = 11.00$  to  $z = 11.01$ ), and  $T_s = T_{\text{CMB}}$  everywhere else, as shown in the top panel of Fig. B3. The HI density is still the same as the default model (calculated from the ionisation fraction  $x_i$ ). We adopt a turbulent velocity of  $v_{\text{turb}} = 100$  km s $^{-1}$ , corresponding to  $\text{FWHM}_\nu = 0.7889$  MHz in the local rest frame. The 21-cm spectra ( $I_L - I_C$ ) in the rest frame of  $z = 11.011, 11.008, \dots, 10.986$ , saved when the radiative transfer calculation has been carried out to these redshift points are presented in the bottom panel. These spectra are color-coded as well as annotated, with the thick bluer lines for higher redshift starting with  $z = 11.011$  and the thin red line with dot marker for lower redshift ending at  $z = 10.986$ . For all the presented spectra, there is a

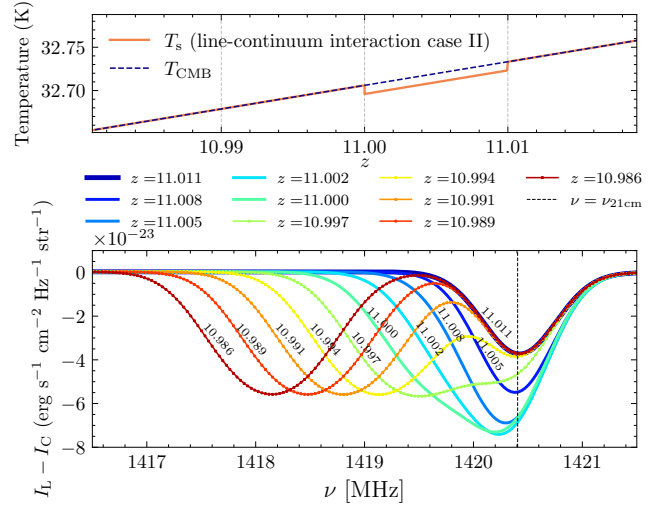


**Figure C1.** Line continuum interaction case II. Similar to case I in Fig. B3, the top panel shows the input spin temperature for the second case of line continuum interaction calculation. The HI density is still the same as in Fig. 1. The spin temperature  $T_s$  is set to be  $0.01$  K lower than  $T_{\text{CMB}}$  between  $z = 11.00$  and  $z = 11.01$ , and  $T_s = T_{\text{CMB}}$  at  $z > 11.01$  or  $z < 11.00$ . The turbulent velocity  $v_{\text{turb}}$  is set to be  $100$  km s $^{-1}$ . This would generate a narrow absorption signal in the local rest frame. The bottom panel shows the spectra calculated with C21LRT in the local rest frame of over redshift  $z = 10.986 - 11.011$ . See main text for the how line continuum interaction shaped these spectra.

Gaussian function shaped dip at  $\nu_{21\text{cm}}$ . This is because the radiative transfer has only been carried out to this redshift (this is the same as the sharp decrease at  $\nu_{21\text{cm}}$  in Fig. 4). The spectrum at  $z = 11.011$  essentially has no 21-cm signal except for the dip. The 21-cm signal then gradually rises near  $\nu_{21\text{cm}}$  first at  $z = 11.008$  to  $z = 11.000$ . These features would be lost if line broadening and radiative transfer effects are not account for. The emission bump then gradually moves towards lower frequency from  $z = 11.000$  to  $z = 10.986$  and the dip gradually recovered to the original shape.

Similarly, we set the spin temperature as  $T_s = T_{\text{CMB}} - 0.01$  K from  $z = 11.00$  to  $z = 11.01$  to create an absorption 21-cm signal, as shown in the top panel of Fig. C1. The 21-cm spectrum also start with a dip centred at  $\nu_{21\text{cm}}$  at  $z = 11.011$  (blue thick line in the bottom layer of the bottom panel). Then true absorption feature first develops near  $\nu_{21\text{cm}}$  at  $z = 11.008$  and gradually widens. The true absorption feature and the original dip due to calculation creates a valley like shape at  $z = 10.997$  (green line with dot marker). Then the absorption feature fully develops and moves towards lower redshift.

For both cases, there was no significant true features at  $z > 11.011$ . The absorption and emission features will continue to move towards lower frequency as radiation propagate towards  $z < 10.986$ . We therefore only present the spectra with  $10.986 < z < 11.011$ . The frequency range in the spectra where the convolution effect between line broadening and radiative transfer with continuum emission is the most prominent is jointly determined by the line profile,  $T_s - T_{\text{CMB}}$ , and the redshift range where  $T_s - T_{\text{CMB}}$  is non-zero. We intentionally adjusted these factors so that the spectra in Fig. B3 and Fig. C1 are clear and straightforward to interpret. The line continuum interaction effects are still present if we adopt a more complicated  $T_s$  and  $x_i$  model, albeit less straightforward for interpretation.

This paper has been typeset from a  $\text{\LaTeX}$  file prepared by the author.